Environmental Technology & Innovation 37 (2025) 103984

Contents lists available at ScienceDirect

Environmental Technology & Innovation

journal homepage: www.elsevier.com/locate/eti

The photocatalytic and antibacterial activity of graphene oxide coupled CoO_x /MnO_x nanocomposites

Heshan Liyanaarachchi [a], Charitha Thambiliyagodage [a,*], Madara Jayanetti [a], Geethma Ekanayake [a], Supuni Wijayawardana [a], Upeka Samarakoon [b]

[a] Faculty of Humanities and Sciences, Sri Lanka Institute of Information Technology, Malabe, Sri Lanka
[b] Department of Nano Science Technology, Faculty of Technology, Wayamba University of Sri Lanka, Kuliyapitiya, Sri Lanka

ARTICLE INFO

Keywords:
Methylene blue
Sunlight
Nanomaterials
Cobalt oxide
Manganese oxide

ABSTRACT

CoO_x and MnO_x metal oxide composites were fabricated via co-precipitation varying the Co:Mn (CM) weight ratio as 4:1, 2:1, 1:1, 1:2 and 1:4, and they hydrothermally coupled with 30 wt% of graphene oxide (GO). XRD analysis revealed the presence of Co_3O_4 and CoO, and Mn_2O_3 and Mn_3O_4 phases in pure CoO_x and MnO_x metal oxides, respectively. The irregularly shaped metal oxide nanocomposites comprised Co_3O_4, Mn_2O_3 and Mn_3O_4 phases and were immobilized on GO. The band gap values of the composites varied in the range of 1.86 – 2.22 eV. The highest photocatalytic activity with a rate constant of 3.5×10^{-3} min^{-1} was obtained with CMG (1:4). The total removal of MB increased by 55.8 % when CM (1:4) were coupled with GO. The rate of photocatalysis was dramatically increased in the presence of $S_2O_8^{2-}$ and was decreased in the presence of EDTA and isopropyl alcohol. The effect of catalyst dosage was determined by varying the weight to 25, 50, 75, and 100 mg, and the dye concentration was varied in the range of 25, 50, 75 and 100 mg/L. The presence of Pb^{2+} and Rhodamine B decreased the photocatalytic activity, while it remained the same in the presence of Cl^- and PO_4^{3-} as co-pollutants. The photocatalytic activity of CMG (1:4) was reduced to 72 % upon using the catalyst for five cycles. All the synthesized nanocomposites exhibited greater sensitivity to the Gram-positive strain than the Gram-negative strains.

1. Introduction

Untreated wastewater from residential, industrial, and commercial sources contributes to water scarcity and quality depletion in aquatic ecosystems. It contains pollutants like pesticides, heavy metals, pharmaceutical waste, dyes, and fertilizers (Rizvi et al., 2024; Iqbal et al., 2024). A wide array of technologies has been developed for dye removal from wastewater to reduce their detrimental environmental effects such as adsorption (Rashid et al., 2021), sedimentation (D. Stickland et al., 2008), filtration: microfiltration (Anis et al., 2019), ultrafiltration (Siagian et al., 2021), nanofiltration (Abdel-Fatah, 2018; Mulyanti and Susanto, 2018) and reverse osmosis (Trishitman et al., 2020) with different types of membranes, chemical treatment: coagulation and filtration (Zhao et al., 2021; Teh et al., 2016), oxidation: chemical oxidation (Ma et al., 2021), UV-assisted oxidation (Khajouei et al., 2022), sunlight based photocatalysis (Thambiliyagodage et al., 2022), fenton's reagent (Bello et al., 2019), photolysis sonolysis (Patidar and Srivastava, 2021), ozone or potassium permanganate (Wang and Chen, 2020), electrochemical: electro-oxidation (Nair et al., 2023),

* Corresponding author.
E-mail address: charitha.t@sliit.lk (C. Thambiliyagodage).

https://doi.org/10.1016/j.eti.2024.103984
Received 29 September 2024; Received in revised form 1 December 2024; Accepted 17 December 2024
Available online 21 December 2024

electro-coagulation (Camcioglu et al., 2014) and electro-degradation (Saba et al., 2021), and biological treatment (Al-Tohamy et al., 2022) including aerobic and anaerobic treatment. The advanced oxidation process (AOP) is a sustainable and viable technology for treating water to remove bio-recalcitrant organic pollutants and inhibit pathogen growth that conventional methods cannot effectively address (Hübner et al., 2024; Saravanan et al., 2021a). The principle of AOP is based on the in-situ generation of reactive oxygen species such as $OH^{\bullet}$, $O_2^{\bullet}$, H_2O_2, and O_3, which can degrade pollutants acting as potent oxidizing agents (Kumari and Kumar, 2023 May). When interacting with organic pollutants, they produce carbon radicals, which may convert into organic peroxyl radicals (ROO) when combined with O_2. All of the radicals undergo additional reactions that result in the generation of other reactive species, such as hydrogen peroxide and superoxide ions, which can cause chemical damage and, in some cases, the mineralization of water (Garrido-Cardenas et al., 2019). Some examples of advanced oxidation techniques are photocatalysis, Fenton, photo-Fenton, ozonation, and electrochemical oxidation. These techniques can efficiently remove dyes without the generation of sludge. This method uses different semiconductor-based photocatalysts, like iron oxide (Fe_2O_3, 2.2 eV) (Bhuiyan et al., 2020; Aslam et al., 2018), ilmenite ($FeTiO_3$, 2.8 eV) (Subha et al., 2022), vanadium oxide (V_2O_5, 2.8 eV) (Ghosh et al., 2018), bismuth oxide (Bi_2O_3, 2.8 eV) (Dai et al., 2014), zinc oxide (ZnO, 3.2 eV) (Roy and Chakraborty, 2021) and titanium dioxide (TiO_2, 3.2 eV) (Mendis et al., 2023). These catalysts have been modified to improve the effectiveness of photocatalytic activity (Natarajan et al., 2018). Titanium dioxide is an effective photocatalyst because of its high quantum yield, stability, and low toxicity. Because of its band gap value of 3.0 eV, the activity of TiO_2 is primarily restricted to the UV region of the electromagnetic spectrum. The process necessitates using an expensive catalyst activation method using artificial light sources, with ultraviolet light being the most commonly used source (Garrido-Cardenas et al., 2019; Zawadzki, 2022). Different photocatalysts have been employed to degrade different dyes. Cu-doped TiO_2/g-C_3N_4 (Mendis et al., 2023) and TiO_2–Fe_3O_4 coupled with graphitic carbon composites (Natarajan et al., 2018) have been used to photodegradation methylene blue. ZnO has been used as the photocatalyst for the degradation of azo dyes (Orange II and Direct Yellow 12) (Zawadzki, 2022; Gouvêa et al., 2000) and some reactive dyes (Remazol Black B and Remazol Brilliant Blue R) (Gouvêa et al., 2000) under UV light. Furthermore, novel photocatalysts have been used for the degradation of dyes: ms-$BiVO_4$ for the degradation of Rhodamine B and Methylene Blue (Guo et al., 2010), dysprosium (Dy) doped WO_3 for the degradation of Rhodamine B (Liu et al., 2007), molybdenum oxides (Bi_2MoO_6 (Martínez-de la Cruz and Obregón Alfaro, 2010), $Bi_2Mo_2O_9$ (La Cruz and Lozano, 2010), $ZrMo_2O_8$ and $NiMoO_4$ (Ghorai et al., 2008)) for the degradation of Methyl Orange, S-N/WO_3 for the degradation of MB (Younas et al., 2024), γ-Fe_2O_3/activated carbon for the degradation of methyl orange (Faheem et al., 2024).

Eliminating microorganisms from water bodies is becoming increasingly popular worldwide to ensure safe and clean drinking water. Water can be contaminated by bacteria, viruses, and protozoans from sources like industrial sludge, urban sewage, and agricultural effluents (Amin et al., 2014). These water-bone pathogenic bacteria are responsible for infectious diseases and can lead to gastrointestinal illness outbreaks (Cabral, 2010; Pandey et al., 2014). The standard chlorine chemical disinfection is carcinogenic and costly, producing harmful by-products like chlorite and chlorate. Ozone and UV disinfection do not leave residual products, but ozone generates organic reaction products, and UV disinfection requires longer exposure times. Low-cost filtration systems like sand and ceramic effectively remove pathogenic bacteria and reduce COD, BOD, and TSS in wastewater. However, effluents cannot be considered sterile due to the presence of pathogenic microorganisms from permeation zone contamination (Al-Gheethi et al., 2018).

As discussed above, numerous metal oxides have been investigated for use as heterogeneous photocatalysts in wastewater treatment. Presently, many researchers have focused on the utilization of carbonaceous materials to improve the photocatalytic performance of semiconductor photocatalysis (Thambiliyagodage et al., 2020). Among them, carbon nanotubes, graphene and graphene-based materials, and carbon quantum dots have been employed. However, graphene and its derivatives have become one of the most promising options (Jamjoum et al., 2021). Due to their excellent electronic properties, graphene and its derivatives act as electron sinkers and electron mediators in nanocomposite materials with metal oxide photocatalysts. They can enhance photocatalytic activity when the catalyst surface is covered with reaction products, preventing surface interaction with incoming pollutant molecules. Furthermore, graphene derivatives can narrow band gap, preventing nanoparticle agglomeration and improving photocatalytic effectiveness (Singh et al., 2020). Numerous studies have reported the photocatalytic degradation of Graphene oxide (GO) and reduced graphene oxide (rGO) nanocomposites. Rhodamine B (RhB), Methylene Blue (MB), and diphenhydramine were all efficiently degraded by the GO–TiO_2 and rGO–TiO_2 composites (Zhang et al., 2017). The BiVO4–rGO composite also demonstrated a notable amount of ciprofloxacin degradation activity (Shi et al., 2021). WO_3–graphene composites showed efficacy against MB and RhB (Thambiliyagodage et al., 2020), while ZnO, in combination with GO and rGO, also degraded Methylene Blue (Qin et al., 2017).

Several available photocatalysts limit their usage only to UV radiation, significantly increasing costs. This is especially because solar light only contains around 5 % of UV radiation; as a result, light energy must be supplied by an external source. Furthermore, it would be highly beneficial if the photocatalyst could have effective photocatalytic activity in visible light. According to our knowledge, the coupling of Mn and Co oxides with graphene oxide for enhanced photocatalytic activity under visible light has not been reported in detail. Further, the antibacterial activity of synthesized nanocomposites on gram-negative and positive bacteria has not been studied before. Here, we report the photocatalytic activity of synthesized nanocomposites by combining the metal oxide in different ratios and coupling with graphene oxide under visible light and the effect of the composites on the growth of the test organisms *Staphylococcus aureus*, *Escherichia coli*, *Klebsiella pneumoniae* and *Pseudomonas aeruginosa*.

2. Methodology

2.1. Chemicals and materials

$CoCl_2$, $MnSO_4$, H_2SO_4 (99.8 %), H_3PO_4 (37.5 %), and H_2O_2 (30 %) were procured from Sigma Aldrich (UK). NaOH pellets and

$KMnO_4$ were purchased from Sisco Research Laboratories (Pvt) Ltd, India. Methylene blue (98 %), Rhodamine B, Phenolphthalein, Methyl orange, Muller Hinton Agar (MHA), and Luria Bertani Broth (LB broth) were purchased from HiMedia Leading Biosciences Company (Maharashtra, India). Graphite was obtained from Bogala, Sri Lanka. In all the experiments, deionized water (DI), with resistivity greater than 18.0 MΩ cm (Millipore Milli-Q system), was used. Chemicals were of analytical grade and utilized without further purification.

2.2. Synthesis

2.2.1. Synthesis of the nanocomposite

The initial step of the process was done via coprecipitation to synthesize CoO_x and MnO_x in the ratios of 1:1, 1:2, 1:4, 2:1, and 4:1 using the salts $CoCl_2$, and $MnSO_4$, in the presence of 1 M NaOH. The resulting oxide solutions were hydrothermally treated at 180 °C for 15 hours to obtain the nanocomposites, which were eventually rinsed with deionized water to get rid of the SO_4^{2-} and Cl^- ions and obtain a neutral pH, followed by drying at 60 °C to remove moisture. The resulting product was annealed at 600 °C for 2 hours at atmospheric conditions. The synthesis procedure was adapted from a modified version of a reported protocol (Thambiliyagodage et al., 2024).

2.2.2. Synthesis of graphene oxide

The optimized Hummer's method was utilized to synthesize graphene oxide using natural graphite powder. Graphite powder and KMnO4 were blended in a 1:3 ratio and combined with an acid mixture containing conc. H_2SO_4 (99.8 %) and conc. H_3PO_4 (37.5 %). After treating the powder with the acid combination, the mixture was stirred at 55 °C for 24 hours. The temperature of the solution was allowed to reach room temperature before 30 % H_2O_2 was added, and it was stirred for five minutes. After obtaining the solid, it was rinsed with deionized water until a neutral pH was reached. Finally, the material was dried at 60 °C until all the moisture was evaporated and stored for further use (Usgodaarachchi et al., 2022).

2.2.3. Fabrication of the nanocomposite

The CoO_x and MnO_x nanomaterials (CoO: MnO, 1:1, 1:2, 1:4, 2:1, 4:1) were then coupled with 30 % graphene oxide via hydrothermal treatment at 180 °C for 12 hours, followed by drying to remove moisture and stored for further analysis (Thambiliyagodage et al., 2024).

2.3. Photocatalytic activity

Photocatalytic activity of the synthesized nanocomposites was evaluated for the degradation of the methylene blue under sunlight. In the experiment, 25 mg of the nanocomposites were shaken in 25 mL of 25 mg/L aqueous solutions for 18 h until the adsorption-desorption equilibrium was reached. The solutions were then decanted and resuspended in 50 mL of 10 mg/L MB and kept in the dark for 30 min. The solutions were subsequently exposed to sunlight, and during that period, aliquots were withdrawn at 15-minute intervals to analyze the samples by taking absorbance readings using a UV–visible spectrophotometer. To study the effect of scavengers, IPA (4 mM) and EDTA (4 mM) were added just before exposing the solutions to sunlight. The effect of persulfate ions was studied by performing photocatalytic experiments in the presence of 1, 2, 4, and 8 mM of persulfate ions. The effect of catalyst dosage was determined by varying the catalyst's weight to 25, 50, 75 and 100 mg, and the effect of the concentration of MB was also studied by varying the MB concentration to 5, 10, 25 and 50 mg/L. The experiments were conducted between 11.00 a.m. and 3.00 p.m. in May 2023, where the lux value varied in the 80,000–1200,000 lux range during the experiments (Thambiliyagodage et al., 2024).

2.4. Antibacterial activity

2.4.1. Preparation of media

The bacterial growth culture media were prepared by mixing Muller Hinton agar and Luria Bertani broth with deionized water, followed by complete sterilization in the autoclave.

2.4.2. Bacterial culture preparation

The gram-negative *E. coli*, *P. aeruginosa*, *K. pneumoniae*, and gram-positive *S. aureus*, serving as the test organisms, were procured from the Medical Research Institute, Sri Lanka. The above microbial cultures were sub-cultured by introducing to the Luria Bertani broth medium and subsequently allowed to grow for 24 hours before the assay. The concentrations of the cultures were then adjusted and diluted to attain a microbial suspension containing 5×10^5 colony-forming units (CFUs)/mL using a UV–visible spectrophotometer for subsequent analysis (Jayanetti et al., 2024).

2.4.3. Agar well diffusion method

Synthesized nanocomposites were weighed (20, 40, and 60 mg) and sonicated in Dimethyl sulfoxide (DMSO) for 1 h. The Mueller Hinton Agar plates were inoculated by spreading the 5×10^5 colony-forming units (CFUs)/mL adjusted microbial inoculum over the entire MHA surface via streaking. Wells were punched aseptically with a sterile cork borer, and about 70 μL of the nanocomposite solution of desired concentrations (20, 40, and 60 mg in 1 mL of DMSO) were introduced into the wells. One well each in a plate was additionally treated with a standard antibiotic (amoxicillin) as the positive control and dimethyl sulfoxide (DMSO) as the negative control. Three duplicates were made for every sample and every kind of bacterium. The prepared agar plates were then incubated for

about 18 h at 37 °C, and the inhibition zones were measured in mm.

3. Material characterization

The scanning electron microscopic (SEM) images were obtained to study the morphology of the materials using a Carl ZEISS EVO 18 RESEARCH instrument. A transmission electron microscope (TEM) (JEOL–JEM-2100) operating with 200 kV characterized the morphology of the synthesized nanocomposites in detail at the nanoscale. X-ray diffraction analysis (XRD) patterns were acquired using the D8 Advance Bruker system, with Cu K α (λ=0.154 nm) anode, varying the 2θ from 5° to 80° at a scan speed of 2 °/min. X-ray photoelectron spectroscopy (XPS) analyzed the nanomaterials' surface chemistry. The Thermo Scientific ESCALAB Xi+X-ray photoelectron spectrometer acquired the survey spectra and higher-resolution spectra of the synthesized catalysts. The samples' diffuse reflectance spectra (DRS) were analyzed using a Shimadzu 1800 UV/ Visible spectrophotometer armed with a precision Czerny-Turner optical system. Measurements were done using a bandwidth of 1.0 nm and a wavelength range of 400–750 nm. The absorbance of the samples was measured using a Shimadzu UV-1990 double-beam UV–visible spectrophotometer.

4. Results and discussion

4.1. XRD

The crystallography of the prepared nanocomposites was determined by analyzing the sample with X-ray diffractometer (Fig. 1). The XRD pattern of the CoO_x nanoparticles shows the presence of both the CoO and Co_3O_4 phases. Peaks at 31.19°, 36.75°, 38.25°, 44.73°, 55.47°, 59.36°, 65.37°, 73.48°, 76.67°, 77.70° which correspond to the (220), (311), (222), (400), (422), (511), (440), (620), (533) and (622) atomic planes of Co_3O_4, respectively (JCPDS No. 74–1656), and the peaks at 36.37°, 42.24°, 61.28°, 73.39°, 77.24° represent the (111), (200), (220), (311), and (222) atomic planes of CoO, respectively (JCPDS No. 78–0431). The interlayer distance of the (311) plane of Co_3O_4, 0.25 nm, is attributed to the crystallite size of 28.26 nm, while the interlayer distance of 0.21 nm with a crystallite size of 31.73 nm corresponds to the (200) plane of CoO. The number of crystal planes in those two oxides is 113 and 151, respectively. The XRD pattern of Mn shows the presence of both Mn_2O_3 and Mn_3O_4 phases. The peaks at 23.33°, 32.54°, 38.42°, 45.39°, 49.57°, 55.39°, and 65.99° are attributed to (211), (222), (400), (332), (431), (440), (622) atomic planes of Mn_2O_3, respectively (ICDD No. 76–0150), and the peaks at 29.18°, 33.17°, 36.28°, 60.09° which are assigned to (112), (103), (211), and (224), of Mn_3O_4, respectively (ICDD No. 080–0382). The interlayer distance of the (440) plane of Mn_2O_3 is 0.17 nm, and the crystallite size is calculated to be 30.80 nm. The interlayer distance of the (103) of Mn_3O_4 is 0.27 nm, corresponding to the crystallite size of 28.13 nm. The number of crystal planes in those oxides are 132 and 104, respectively. It was observed that the highest intense peak of CoO (200) was not present in any of the metal oxide nanocomposites abbreviated as CM, suggesting the absence of a CoO phase in them. However, Co_3O_4, Mn_2O_3, and Mn_3O_4 oxides were present in all the composites. The XRD pattern of GO exhibits the characteristic peak at (001) at 10.44°. The d spacings, crystallite size and the number of crystalline planes of each oxide in each nanocomposite prepared are tabulated in Table 1.

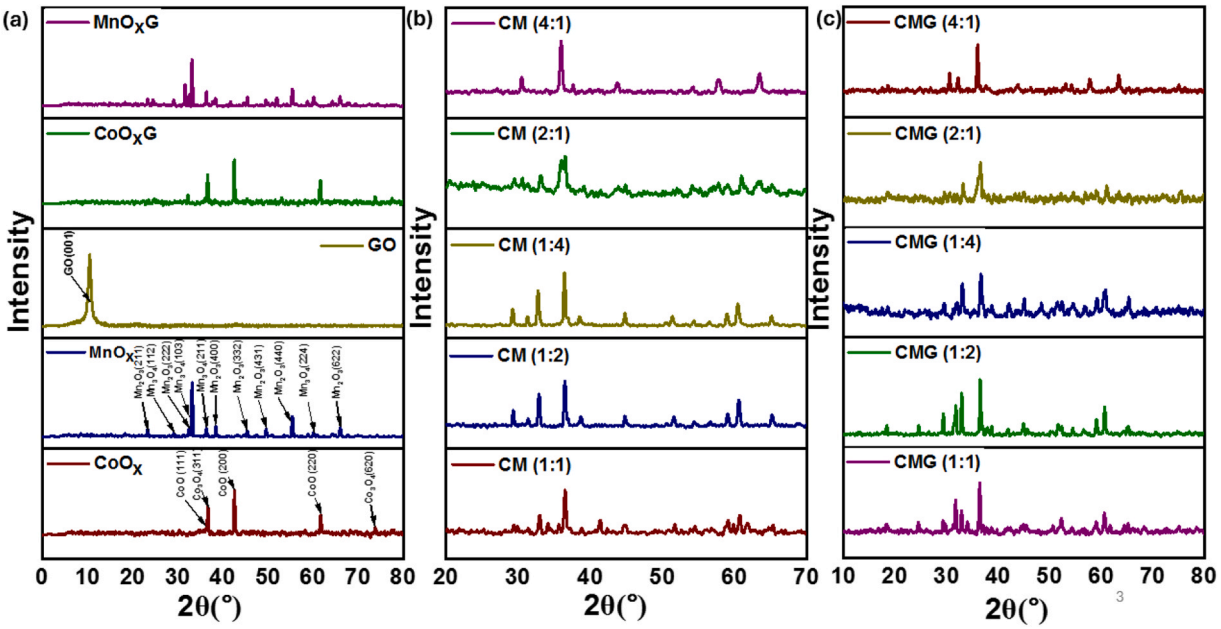

Fig. 1. The XRD patterns of (a) CoO_x, MnO_x, GO, CoO_xG, MnO_xG (b) CM composites (c) CMG composites.

4.2. UV-Visible spectroscopic analysis

The optical absorption behaviour of the synthesized photocatalysts was determined by obtaining the UV–visible spectra. The absorption spectra of the synthesized nanocomposites showed visible range absorption, as shown in Supplementary Fig. 1 where the absorption edges lie greater than 540 nm in all the samples. Tauc plots were composed to determine the band gaps using the formula below.

$(\alpha hv)^n = A(hv\text{-}Eg)$

Where hv, A, Eg and α represent the photon energy, absorption coefficient, band gap energy and a constant, respectively. n = 2 denotes the direct transitions, and n = 1/2 indicates indirect transitions. The plots indicating the direct transitions are shown in the Supplementary Fig. 2, and the plots showing the indirect transitions are exhibited in Fig. 2. The behaviour of the plots suggests that the fabricated nanocomposites follow indirect transitions. The band gap values of CoO_x and MnO_X were quite similar, 1.86 and 1.88 eV, respectively. It was noted that the band gap decreased with increasing Co content in CoO_x:MnO_x composite, where a band gap of ~2.22 eV was obtained for CM 1:1, 1:2, 1:4, whereas for both CM 2:1 and 4:1, the band gap was calculated to be 1.93 eV. The band gap of CoO_x and MnO_X coupled with GO was found to be 1.92 eV, and the band gap of CM coupled with GO was also obtained at 1.92 eV in all samples. The size and shape of the nanomaterial also affect a photocatalyst's band gap in addition to the semiconductor's band alignment. Band gap and particle size are usually inversely linked. The size of the nanoparticles significantly impacts the band gap, where the band gap values increase as the particle size decreases. The band gap between the valence and conduction bands widens when the particle's size decreases because electrons in the conduction band and holes in the valence band are more constrained. The shape of the nanomaterials affects the band gap values. The volume-to-surface area ratio is impacted by changes in the nanomaterials' size and shape, which, in turn, influences the number of surface atoms and, ultimately, the cohesive energy. As a result, the band gap varies at the nanoscale due to the change in size and shape. Thus, several factors contributed to the band gap values that were found.

4.3. XPS analysis

XPS analyzed the surface of the synthesized nanomaterials to study the surface environments. The survey spectra of CM (1:4) and CMG (1:4) shown in Fig. 3(a) and (b), respectively, indicate the presence of C, O, Co and Mn in the samples. The higher resolution XPS spectrum of C 1 s of CM (1:4) shown in Fig. 3(c) was deconvoluted to four peaks at 283.8, 284.5, 285.6 and 286.7 eV, which are assigned to the metal-C (Co/Mn-C), sp^2 hybridized C-C, C-O and O═C-O. The same chemical bonds were present in CMG (1:4), represented by the peaks at 282.6, 284.5, 286.1 and 287.9 eV (Fig. 3(d)) (Greczynski and Hultman, 2020). The higher resolution spectrum of O 1 s of (CM 1:4) (Fig. 3(e)) was deconvoluted to five peaks at 529.2, 529.7, 530.3, 531.1 and 532.7 eV, which are attributed to O in Co_3O_4, Mn^{2+}-O, Mn^{3+}-O, H_2O/OH, and Mn^{4+}-O, respectively (Tian et al., 2020; Zhang et al., 2020). The higher resolution spectrum of O 1 s of CMG (1:4) (Fig. 3(f)) indicates the presence of Co^{3+} -O, Mn^{2+}-O, H_2O/OH, and Mn^{4+}-O by the peaks appearing at 528.1, 529.8, 531.1 and 532.7 eV, respectively. The higher resolution spectrum of Co 2p of CM (1:4) (Fig. 3(g)) shows the spin-orbital coupling splitting the spectrum mainly into two peaks corresponding to $2p_{3/2}$ and $2p_{1/2}$. It represents the presence of Co^{3+} on the surface of the nanomaterial with $2p_{3/2}$ and $2p_{1/2}$ positioning at 781.4 and 797.1 eV, respectively, and their corresponding satellite peaks at 786.9 and 802.8 eV, respectively. In addition to Co^{3+}, the presence of Co^{4+} was apparent in the higher resolution spectrum of Co 2p of CMG (1:4) (Fig. 3(h)) by the peak at 783.5 eV (Haunold and Rupprechter, 2021). The higher resolution spectrum of Mn of CM (1:4) exhibited in Fig. 3(i)) was split mainly into two peaks as $2p_{3/2}$ and $2p_{1/2}$, due to the spin-orbital coupling. The figure

Table 1
Crystallographic parameters of the synthesized nanomaterials.

Sample	Crystal Plane	2θ (°)	Crystallite size (L) (nm)	d spacing (nm)	Number of crystalline planes (L/d)
CoO_x	Co_3O_4(311)	36.64	28.36	0.25	113
	CoO (200)	42.53	31.73	0.21	151
MnO_x	Mn_3O_4 (103)	33.15	28.13	0.27	104
	Mn_2O_3 (440)	55.37	30.80	0.17	181
CM (1:1)	Co_3O_4 (311)	36.5	33.28	0.25	133
	Mn_3O_4 (103)	32.99	24.29	0.27	90
	Mn_2O_3 (440)	53.39	32.94	0.17	194
CM (1:2)	Co_3O_4 (311)	36.46	31.19	0.25	125
	Mn_3O_4 (103)	32.90	24.90	0.28	89
	Mn_2O_3 (440)	54.30	26.76	0.17	157
CM (1:4)	Co_3O_4 (311)	36.42	31.79	0.25	127
	Mn_3O_4 (103)	32.75	30.12	0.27	112
	Mn_2O_3 (440)	54.39	25.97	0.17	153
CM (2:1)	Co_3O_4 (311)	36.51	28.85	0.25	115
	Mn_3O_4 (103)	33.13	29.51	0.27	109
	Mn_2O_3 (440)	55.19	34.56	0.17	203
CM (4:1)	Co_3O_4 (311)	35.96	24.85	0.25	99
	Mn_3O_4 (103)	33.85	28.79	0.26	111
	Mn_2O_3 (440)	54.27	28.23	0.17	166

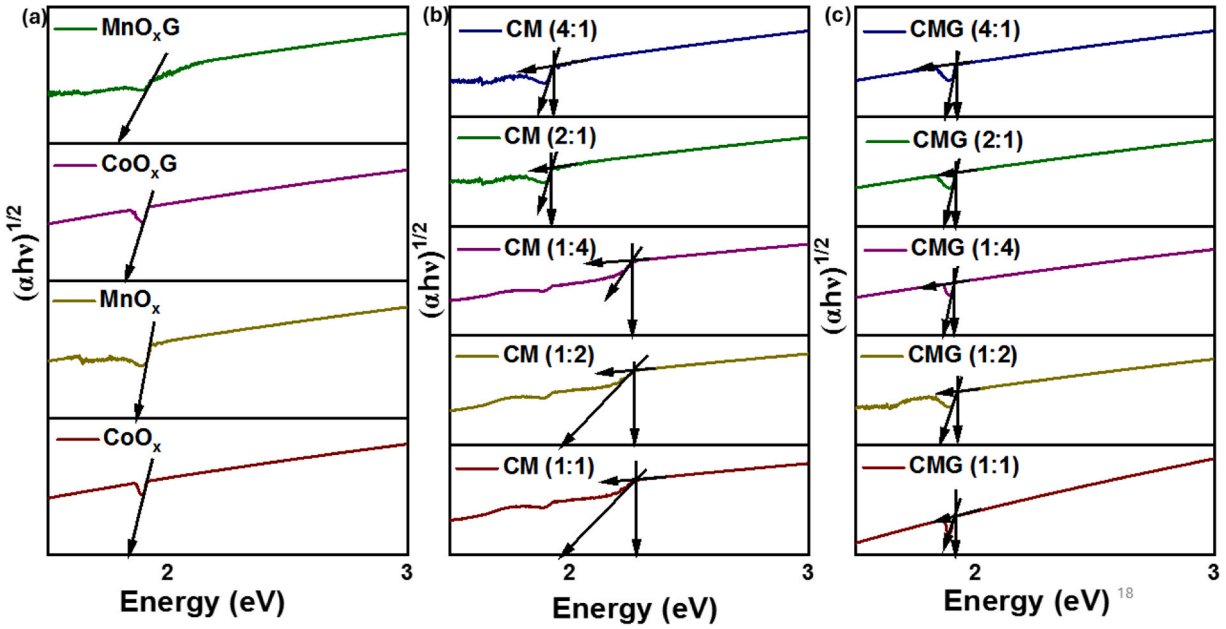

Fig. 2. Tauc plots showing the indirect transitions of (a) CoO_x, MnO_x, GO, CoO_xG, MnO_xG (b) CM composites (c) CMG composites.

further shows the presence of Mn^{2+}, Mn^{3+} and Mn^{4+} by the $2p_{3/2}$ peaks centred at 640.7, 641.7 and 643.1 (Dai et al., 2021). XRD analysis did not reveal the presence of any Mn oxides at its + 4 oxidation state. Therefore, it can be assumed that the surface of the metal oxide nanomaterials contains Mn^{4+}, but it has not been crystallized, or though MnO_2, oxide of Mn which corresponds to + 4 oxidation state, is present, the concentration is low to be detected by XRD. The same chemical environment was observed in the higher resolution spectrum of Mn of CMG (1:4) (Fig. 3(j)).

4.4. Morphological analysis

SEM and TEM images were collected to study the morphology of the synthesized nanocomposites. The oxidised graphite lamella structure, which is crumpled and wrinkled, is seen in the GO image (Fig. 4(a)). The margins of the newly formed individual GO sheets, including their kinked and crumpled structure, are easily distinguished from the folded uniform graphene sheets. Where oxidation happens at the edges and surface of the graphite flakes, wrinkles are created by oxygenated groups that are present on the graphite oxide (GO). The interlayer distance rises due to additional oxygenated groups between the sheets as oxidation continues to the middle of the carbon. The SEM image of CoO_x and MnO_X (Fig. 4(b) and (c)) shows irregular nanoparticles which are interconnected at the edges, resulting in aggregation due to the Oswald ripening that occurs during the hydrothermal treatment. Irregularly shaped nanoparticles of CoO_x and MnO_X were distributed on GO matrix, as shown in SEM images Fig. 4(d) and (e), respectively. The SEM images of CM 1:1, 1:2, 1:4, 2:1, and 4:1 given in Fig. 4(f), (g), (h), (i), and (j), respectively, show that irregularly shaped nanostructures are abundantly present with some heavily aggregated metal oxides which have formed macrostructures of different shapes. The SEM images of CMG 1:1, 1:2, 1:4, 2:1, and 4:1 shown in Fig. 4(k), (l), (m), (n), and (o) reveal the presence of aggregated nanostructures of the CoO_x and MnO_X in which the GO sheets are not apparent as they are covered with metal oxides. This is due to the low percentage of GO present (30 % by weight) compared to the metal oxides in a given sample. The TEM image of CMG 1:4 (Fig. 4(p)) was collected to study the morphology of the nanocomposites in more detail, where the heterogeneous distribution of aggregated nanoparticles on GO sheets was apparent. Hence, it is evident that the metal oxide nanostructures are not uniformly distributed on the GO matrix. HRTEM images of CMG 1:4 are shown in Fig. 4 (Q) and (R), in which the atomic layer arrangement is clearly shown with d spacings of 0.5007 nm and 0.4900 nm, respectively.

4.5. Photocatalysis

Kinetics of adsorbing MB to the synthesized materials were studied using 20 mg of the material with 25 mg/L of MB solution shaking under dark conditions. The variation of A/A_0 with time of GO, CoO_x, MnO_X, CoO_xG and MnO_XG is shown in Fig. 5(a), while that of CM and CMG are shown in Fig. 5(b) and (c), respectively. All the samples reached the equilibrium on or before 5 hours due to the saturation of the adsorption sites. CoO_x and MnO_X have not significantly adsorb MB, where a reduction of 3.4 % and 1.0 % absorbance resulted even after 5 hours of incubation.

GO adsorbs a considerable amount of MB due to the oxygen-rich functional groups present on the surface. The adsorption is greater than that of metal oxides but lesser than that of metal oxide-GO composites. GO has more active sites to adsorb than the pure metal

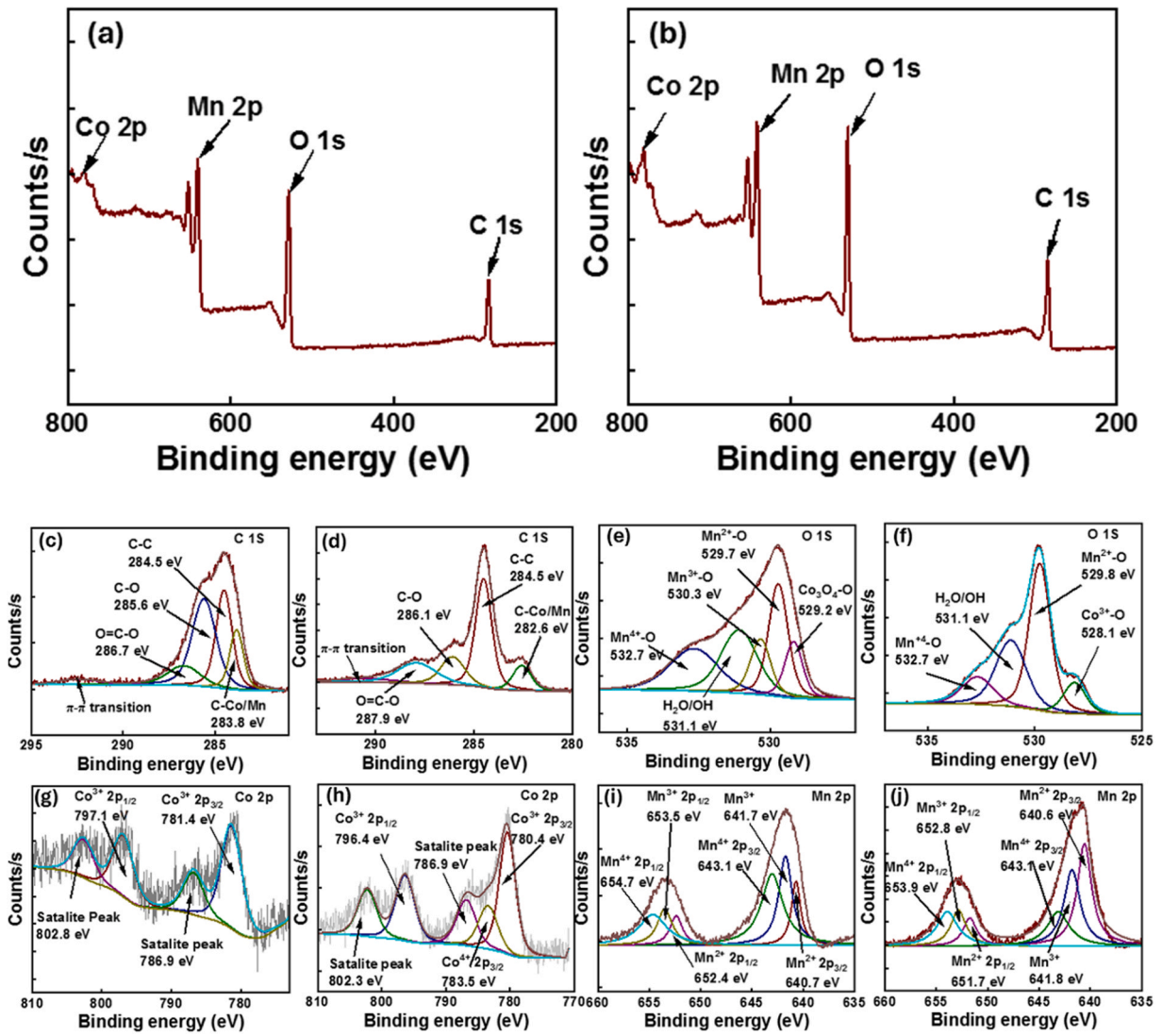

Fig. 3. Survey spectra of (a) CM (1:4) and (b) CMG (1:4), the higher resolution spectra of C 1 s of (c) CM (1:4) and (d) CMG (1:4), of O 1 s of (e) CM (1:4) and (f) CMG (1:4), of Co 2p of (g) CM (1:4) and (h) CMG (1:4), of Mn 2p of (i) CM (1:4) and (j) CMG (1:4).

oxides but the metal oxide-GO composites have more active sites than GO. The same behaviour was observed with the metal oxide composites, where a reduction in absorbance of 7.7, 5.7, 5.9, 7.1 and 3.8 % were obtained with CM 1:1, 1:2, 1:4, 2:1, and 4:1, respectively. This is due to the limited adsorption sites available on the surface of the metal oxide composites. The adsorption drastically increased with the incorporation of GO to the synthesized metal oxides and metal oxide composites, where an increase of 52.3 % and 43.5 % in adsorption resulted in CoO_x and MnO_X after coupling with GO and an increase of 34.5, 56, 55.8, 53.3 and 26.6 % were obtained with CM 1:1, 1:2, 1:4, 2:1, and 4:1, respectively, after performing the same. The same behaviours of the adsorption of MB to the synthesized materials are further supported by the adsorption capacities calculated using the second-order kinetics model. The adsorption capacities of CoO_x, MnO_X, and CoO_xG (0.09247 and 0.08968 mg/g, respectively) increased to 0.20495 and 0.15513 mg/g upon coupling with GO. The same behaviour was observed in CM samples, where the adsorption capacity greatly enhanced once coupled with GO. For example, the adsorption capacity of CM 1:1 (0.09587 mg/g), which shows the highest adsorption capacity among the CM samples, increased to 0.15852 mg/g, which is a 40 % increase in the adsorption capacity. Hence, it is evident that GO plays a significant role in adsorbing MB due to the presence of oxygen-rich functional groups like COOH, OH, C═O, C-O-C, and lactones introduced via acid treatment.

The first-order kinetics plots of CoO_x, MnO_X, CoO_xG and MnO_XG are shown in Fig. 6(a), whereas the same of CM and CMG composites are exhibited in Fig. 6(b) and (c), respectively. The second-order kinetics plots of CoO_x, MnO_X, CoO_xG and MnO_XG are shown in Fig. 6(d), while those of CM and CMG composites are given in Fig. 6(e) and (f), respectively. Both kinetics models' respective rate constant and R^2 values are tabulated in Table 2. According to the R^2 values, the adsorption of MB to the composites follows second-

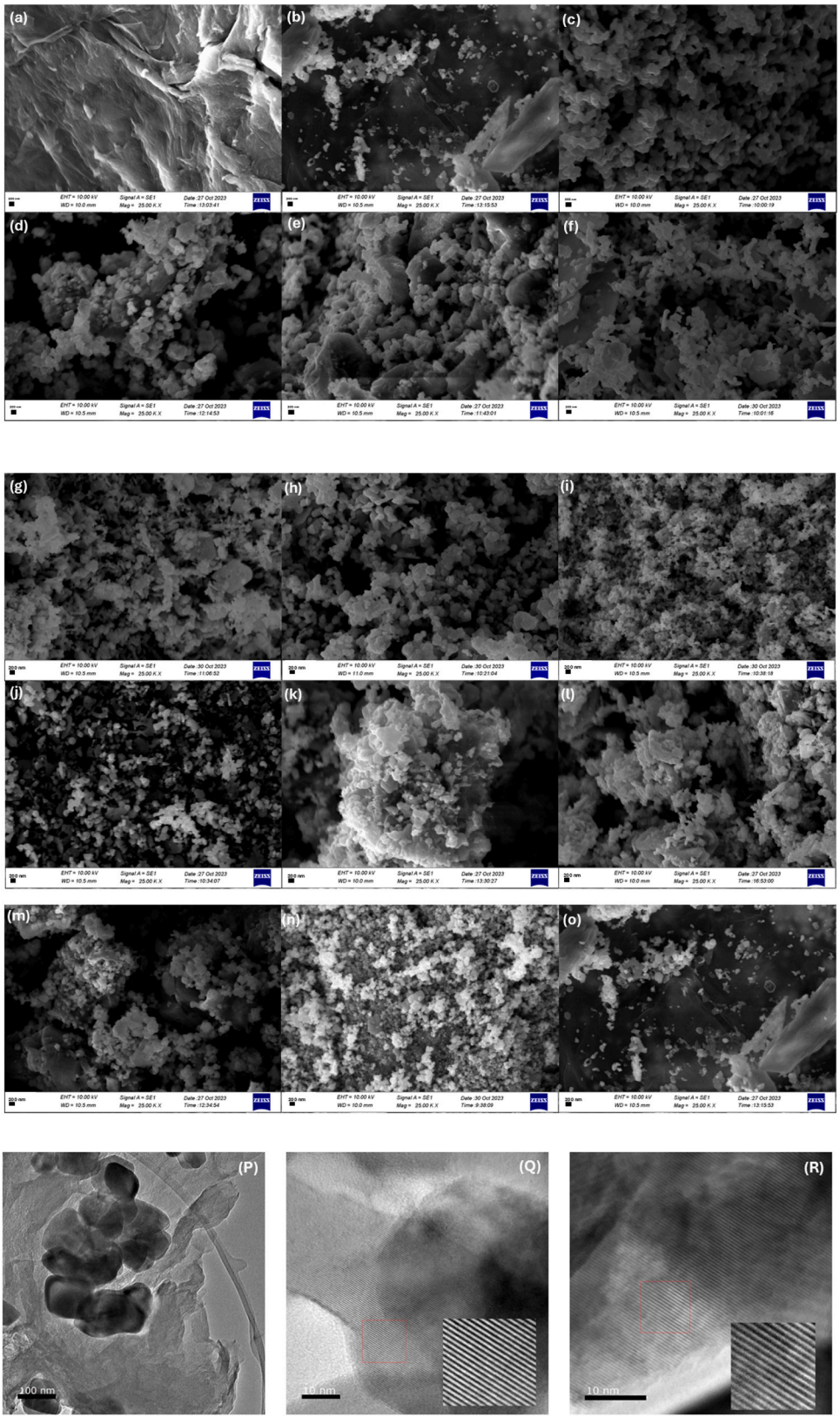

Fig. 4. SEM images of (a) GO, (b) CoO_X, (c) MnO_X, (d) CoO_XG, (e) MnO_XG, (f) CM 1:1, (g) CM 1:2, (h) CM 1:4, (i) CM 2:1, (j) CM 4:1, (k) CMG 1:1, (l) CMG 1:2, (m) CMG 1:4, (n) CMG 2:1, (o) CMG 4:1, (p) TEM image of CMG 4:1 (Q) and (R) HRTEM Images of CMG 1:4.

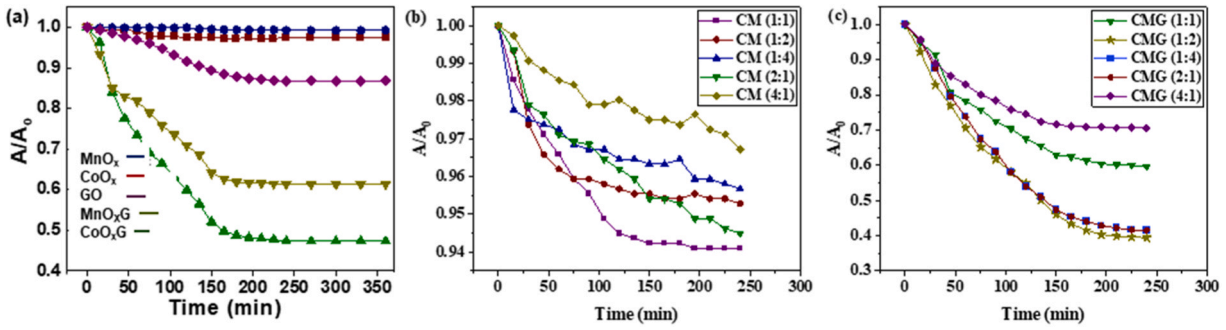

Fig. 5. The variation of A/A_0 with time of (a) CoO_x, MnO_x, GO, CoO_xG, MnO_xG (b) CM composites (c) CMG composites.

order kinetics, suggesting the chemisorption of MB molecules to the adsorbent surface. As discussed above and shown in XPS analysis, GO bears oxygen-rich functional groups, which render a negative charge to the adsorbent surface and facilitate electrostatic interaction with positively charged MB molecules, forming strong bonds between adsorbent and adsorbates. The π-π interactions that occur between the aromatic rings of GO and MB molecules further enhance the chemical interactions.

The reduction in absorbance during the photocatalysis in the presence of CMG (1:4) is shown in Supplementary Fig. 3. It is evident that with no appearance of any other peak and only the reduction of the peak of interest, MB reduction has occurred without forming any other isomers. The variation of A/A_0 of the photocatalytic activity of CoO_x, MnO_X, CoO_xG and MnO_XG is shown in Fig. 7(a), and that of CM and CMG samples are exhibited in Fig. 7(b) and (c), respectively. In general, they indicate that the least reduction of absorbance and, hence, the least photocatalytic performance resulted in the presence of CM (4:1) in which only 29 % of MB was converted. In contrast, the highest photocatalytic conversion of 63 % MB was obtained in the presence of CMG (1:4).

MB doesn't degrade upon exposure to sunlight without any catalyst, as shown in Fig. 8(a). The first-order kinetic plots showing the photocatalytic activity of GO, CoO_x, MnO_X, CoO_xG, and MnO_XG are shown in Fig. 8(a), and those of CM and CMG materials are shown in Fig. 8(b) and (c). Though GO could adsorb MB, it is catalytically inactive in degrading MB because GO cannot generate the free radicals required for photodegradation. The lowest rate of photodegrading the MB (1.7×10^{-3} min^{-1}) resulted in the presence of CoO_x and CoO_xG, while the highest rate constant obtained in the presence of CMG 1:4. A significant difference in the rate constant resulted in coupling with GO except in the presence of CM (1:4) where the rate constant almost doubled compared to that of CM (1:4) (1.9×10^{-3}

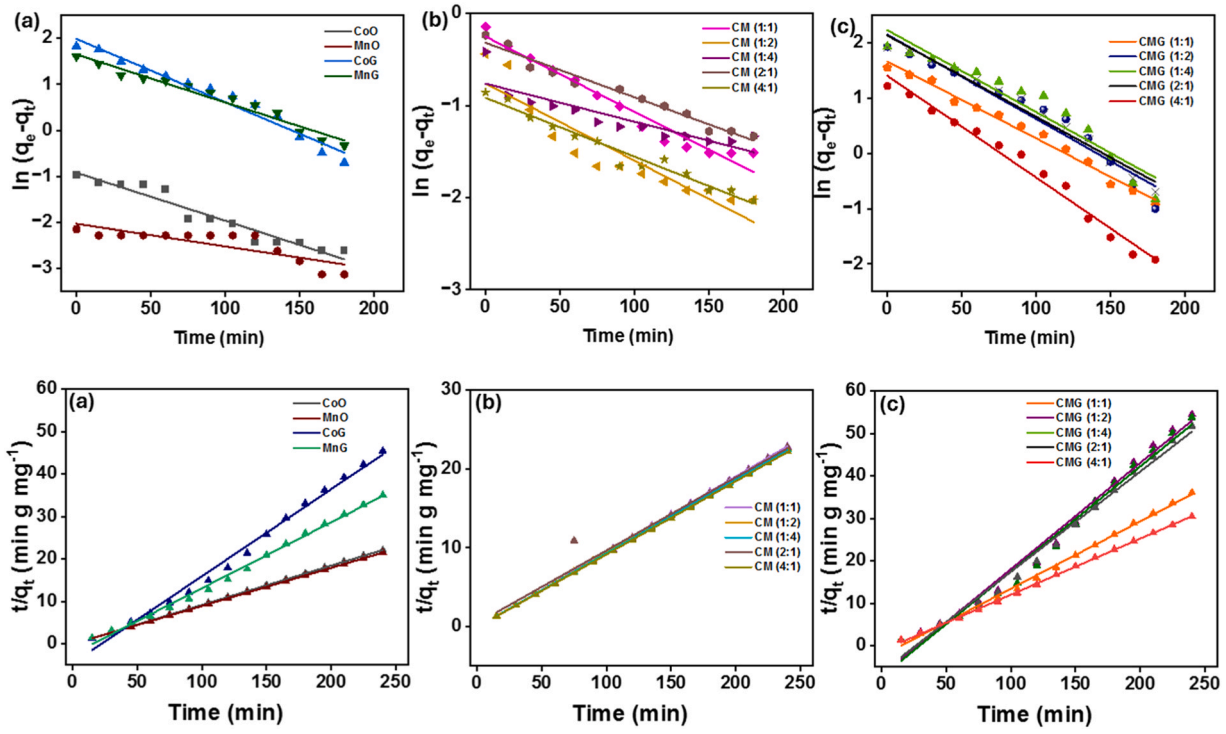

Fig. 6. First-order adsorption kinetics of (a) CoOx, MnOx, GO, CoOxG, MnOxG, (b) CM composites, (c) CMG composites. Second-order adsorption kinetics of (d) CoOx, MnOx, GO, CoOxG, MnOxG, (e) CM composites (f) CMG composites.

Table 2
Kinetic parameters of adsorption of MB to the adsorbents.

Compound	1st order Rate (min^{-1})	R^2	2nd order Rate (min^{-1})	R^2	Q_e (mg/g)
CoO_x	1.04×10^{-2}	0.938	1.14×10^{-1}	0.999	0.09247
MnO_x	4.90×10^{-2}	0.964	9.19×10^{-3}	0.999	0.08968
Co_xOG	1.37×10^{-2}	0.965	1.01×10^{-2}	0.991	0.20495
Mn_xOG	1.03×10^{-2}	0.964	6.44×10^{-2}	0.995	0.15513
CM (1:1)	8.1×10^{-3}	0.960	1.33×10^{-1}	0.999	0.09587
CM (1:2)	8.3×10^{-3}	0.851	1.02×10^{-1}	0.999	0.09424
CM (1:4)	4.1×10^{-3}	0.783	9.88×10^{-2}	0.999	0.09375
CM (2:1)	5.9×10^{-3}	0.972	8.81×10^{-2}	0.979	0.09249
CM (4:1)	6.3×10^{-3}	0.963	7.52×10^{-2}	0.999	0.09260
CMG (1:1)	1.39×10^{-2}	0.987	1.53×10^{-2}	0.997	0.15852
CMG (1:2)	1.52×10^{-2}	0.949	9.01×10^{-3}	0.984	0.24969
CMG (1:4)	1.48×10^{-2}	0.924	8.46×10^{-3}	0.980	0.24742
CMG (2:1)	1.47×10^{-2}	0.977	9.02×10^{-3}	0.988	0.23599
CMG (4:1)	1.84×10^{-2}	0.981	1.47×10^{-2}	0.999	0.13210

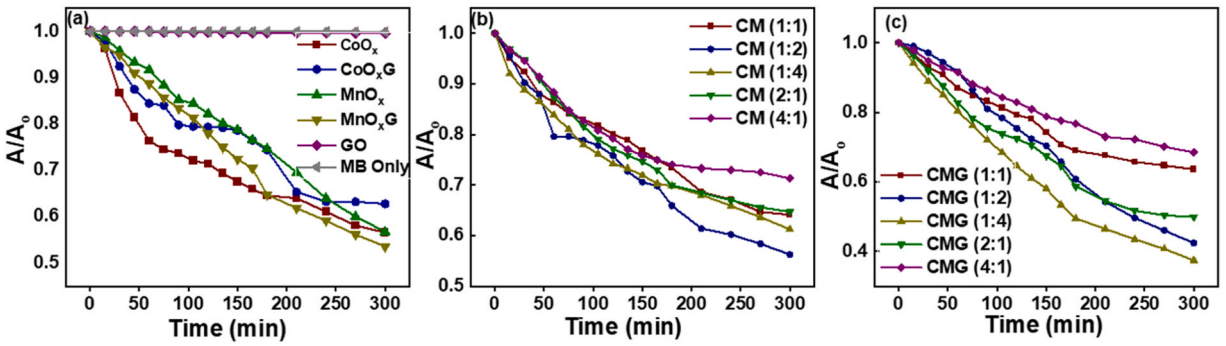

Fig. 7. The variation of A/A_0 with a time of photocatalysis of (a) CoOx, MnOx, GO, CoOxG, MnOxG, (b) CM composites, (c) CMG composites.

min^{-1}) in CMG (1:4) (3.5×10^{-3} min^{-1}). The main reason for obtaining similar rate constants even after coupling with GO, which results in a higher reduction in absorbance with time and reveals higher removal of MB, is related to the number of adsorption sites present in GO. Once the catalyst is exposed to sunlight after shaking in the dark, the rate of photodegrading MB molecules results to be lower as the catalyst, the metal oxide or the metal oxide composite, initially degrades the already absorbed MB molecules. As the number of MB molecules adsorbed to GO increases, the time taken to degrade them would be higher. With time, once the adsorption sites are vacant with the photodegradation of the already adsorbed MB molecules, new MB molecules reach the active sites and start to adsorb, which will eventually be subjected to photodegradation. Hence, the overall photodegradation rate is low, but the total removal of MB molecules would be higher when the metal oxide and metal oxide composites are coupled with GO. This observation was quite apparent with all samples coupled with GO. Further, the photocatalytic activity of some of the samples remains the same, or there is no significant difference due to the resulting band gap values as discussed in DRS-UV-Vis analysis, where similar band gaps were obtained for different samples. Moreover, the aggregation of the particles shown, especially in SEM analysis, would lead to approximately similar surface area. The catalytic reaction takes place at the surface of the catalyst, which is the nanocomposite, and having similar surface areas would lead to similar activities though the ratios or the composition change (Che and Bennett, 1989). Furthermore, small

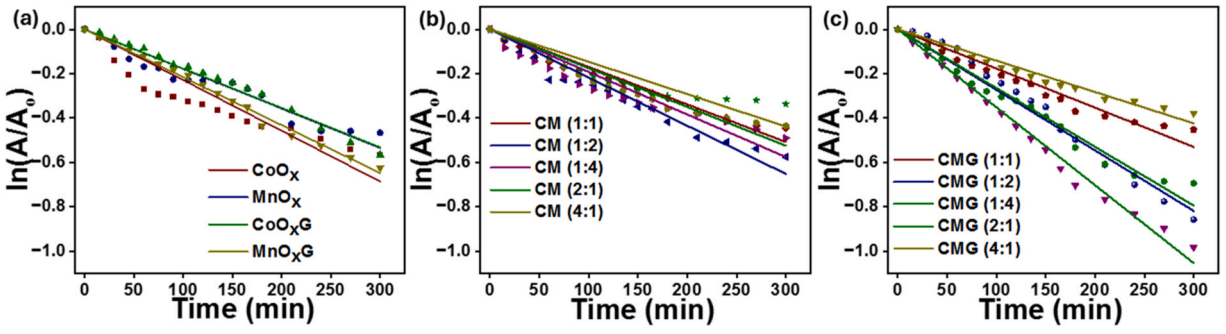

Fig. 8. The first order kinetics plots of photocatalysis of (a) CoOx, MnOx, GO, CoOxG, MnOxG, (b) CM composites, (c) CMG composites.

differences in the surface areas resulting from the aggregation of the nanoparticles and heterogeneous distribution of the nanoparticles on the GO surface would lead to no to small changes in the photocatalytic activity. Interestingly, the surface of the nanocomposites is oxidized with different oxidation states, as revealed by the XPS analysis, which leads to differences in the valence states and electron densities. Surface chemistry significantly impacts the photocatalytic activity (Konsolakis, 2016). Precisely, as shown in the XRD analysis, the crystallite size, interlayer spacings and number of crystalline planes differ without a trend. The crystal nature of the material plays a major role in catalysis, affecting reactivity and selectivity. Differences in the crystal's nature affect the electronic stats, mean free path, and work function (Kang et al., 2024). Hence, different crystallographic parameters would have contributed to the obtained photocatalytic activity. Therefore, it is evident that the material morphology, crystal nature, surface chemistry, and band alignments characterized by many techniques affect the photocatalytic activity. The rate constants and the corresponding R^2 values for the photodegradation of MB in the presence of the catalysts synthesized are tabulated in Table 3.

4.6. The effect of persulfate ions

The effect of the presence of persulfate on the photocatalytic activity was choosing the best-performing photocatalyst CMG (1:4) (Fig. 9). The photocatalytic activity was expected to increase in the presence of persulfate in the presence of persulfate ions due to the production of $SO_4^{\bullet}$ and $OH^{\bullet}$ as follows,

$$S_2O_8^{2-} + e^- \rightarrow SO_4^{\bullet} + SO_4^{2-}$$

$$SO_4^{\bullet} + OH^- \rightarrow SO_4^{2-} + OH^{\bullet}$$

$$S_2O_8^{2-} + h\nu \rightarrow 2\ SO_4^{\bullet -}$$

$$S_2O_8^{2-} + O_2^{\bullet} \rightarrow SO_4^{2-} + SO_4^{\bullet} + O_2$$

The persulfate concentration was varied as 1, 2, 4 and 8 mM, where the rate constant for the photodegradation of MB increased from 3.8×10^{-3} min^{-1} to 2.1×10^{-2}, 3.0×10^{-3}, 3.3×10^{-3}, and 3.3×10^{-3} min^{-1} with increasing concentrations of the persulfate ions from 1 to 8 mM as stated above, respectively. It could be seen that the photocatalytic activity increased with increasing persulfate concentration due to the production of more and more radicals. The photocatalytic activity remains the same, though the persulfate concentration was doubled from 4 to 8 mM. A portion of the persulfate will contribute to producing free radicals once the concentration exceeds this threshold. The excess will reduce the time MB and free radicals can come into contact with, reducing photocatalytic activity. Furthermore, as the following equations demonstrate, sulfate and hydroxyl radicals tend to quench at larger concentrations of persulfate ions.

$$S_2O_8^{2-} + SO_4^{\bullet} \rightarrow SO_4^{2-} + S_2O_8^{\bullet}$$

$$S_2O_8^{2-} + OH^{\bullet} \rightarrow OH^- + S_2O_8^{\bullet}$$

Furthermore, the following interaction between radicals becomes more significant at higher concentrations, lowering the availability of free radicals and, consequently, any photocatalytic activity.

$$SO_4^{\bullet} + SO_4^{\bullet} \rightarrow 2SO_4^{2-}$$

$$OH^{\bullet} + OH^{\bullet} \rightarrow H_2O_2$$

$$SO_4^{\bullet} + OH^{\bullet} \rightarrow HSO_4^- + ½\ O_2$$

Table 3
Kinetic parameters of photocatalysis of the synthesized nanocomposites.

Compound	1st order K (min^{-1})	R^2
CoO_x	2.2×10^{-3}	0.955
MnO_x	1.7×10^{-3}	0.980
CoO_xG	1.7×10^{-3}	0.994
MnO_xG	2.1×10^{-3}	0.997
CM (1:1)	1.7×10^{-3}	0.987
CM (1:2)	2.1×10^{-3}	0.984
CM (1:4)	1.9×10^{-3}	0.966
CM (2:1)	1.7×10^{-3}	0.979
CM (4:1)	1.4×10^{-3}	0.952
CMG (1:1)	1.7×10^{-3}	0.987
CMG (1:2)	2.7×10^{-3}	0.989
CMG (1:4)	3.5×10^{-3}	0.996
CMG (2:1)	2.6×10^{-3}	0.992
CMG (4:1)	1.4×10^{-3}	0.992

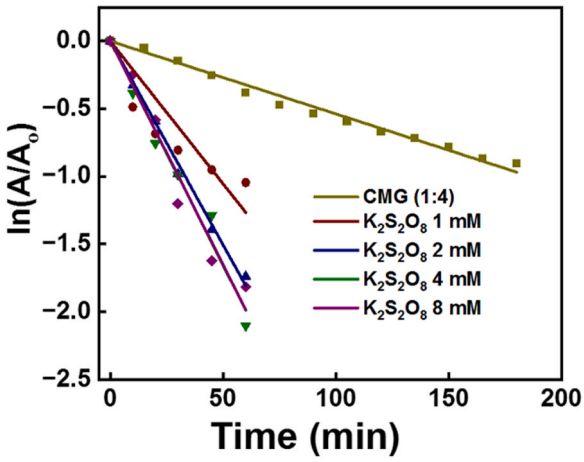

Fig. 9. The effect of persulfate ions on photocatalysis at varying concentrations.

4.7. The effect of scavengers

The effect of radical scavenging reagents EDTA (4 mM) and IPA (4 mM) was tested on the photocatalytic activity of best-performing CMG (1:4) (Fig. 10). The rate constant for the photodegradation of MB was reduced to 2.3 x 10^{-3} and 1.7 x 10^{-3} min^{-1} in the presence of EDTA and IPA, respectively, which is a reduction of 40 % and 55 % compared to the rate constant of CMG (1:4) without any scavenging reagents (3.3 x 10^{-3} min^{-1}). EDTA and IPA scavenge holes and $OH^{\bullet}$, respectively, limiting the reaction. It is worth noting that a similar concentration of persulfate ions (4 mM) increased the rate of the reaction by 88 %.

4.8. The effect of the weight of the photocatalyst

The effect of the catalyst dosage on the photocatalytic activity was determined using the CMG (1:4) catalyst (Fig. 11). The weight of the catalyst varied as 25, 50, 75 and 100 mg, where the rate constants were obtained as 3.5 × 10^{-3}, 3.4 × 10^{-3}, 4.6 × 10^{-3} and 1.9 × 10^{-3} min^{-1}, respectively. There was no change in the rate constant when the catalyst dosage was increased from 25 mg to 50 mg. The rate constant increased by 26 % with the increase of the catalyst weight from 50 mg to 75 mg. This is due to increased active sites with increasing catalyst weight. Further, the concentration of the radicals produced increased due to the increase in the production of the charge carriers by the catalyst with increasing weight of the catalyst. However, the reaction rate decreased with a further catalyst increase to 100 mg by 46 %. The amount of accessible active sites exposed to the reactant MB molecules is reduced when catalyst particles collide and obscure one another's active sites. Additionally, the process that lowers radical generation eventually lessens MB oxidation and also limits the reach of photons produced by the visible light source. Furthermore, as indicated by reaction number, O_2 is produced. It traps the catalyst's surface, which limits the amount of MB molecules that can reach it and reduces the overall amount of MB that has been destroyed.

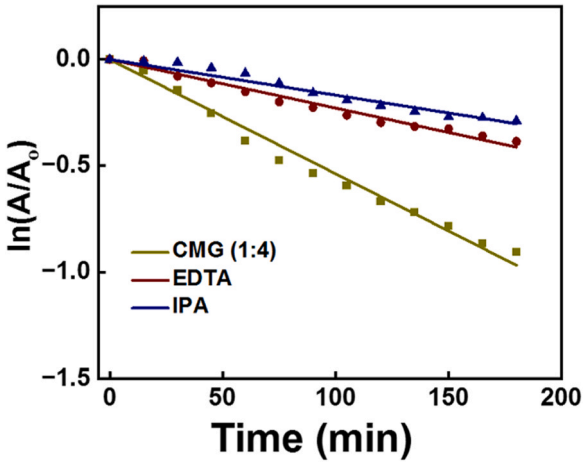

Fig. 10. The effect of scavengers on photocatalytic activity.

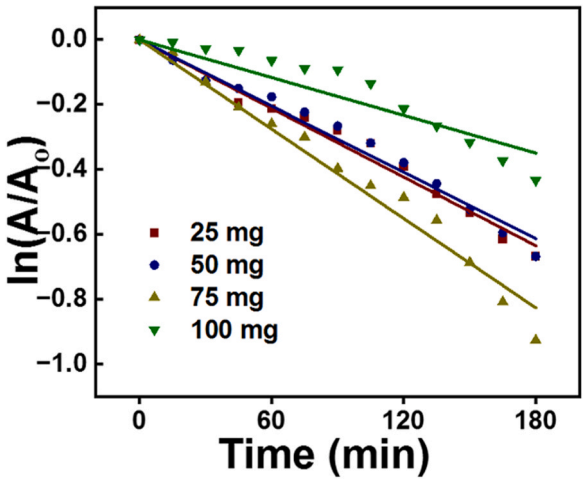

Fig. 11. The effect of the weight of the catalyst on photocatalysis.

4.9. The effect of the MB concentration

The effect of the MB concentration on the photocatalytic activity was determined by varying the concentration of MB to 5, 10, 25 and 50 mg/L (Fig. 12). The rate constant increased from 3.1×10^{-3} to 4.0×10^{-3} min^{-1} once the concentration increased from 5 to 10 mg/L. The rate constant almost remained the same (3.9×10^{-3} min^{-1}) when the concentration of MB increased to 25 mg/L and reduced to 2.6×10^{-3} min^{-1} when the MB concentration increased to 50 mg/L. More molecules tend to adsorb on the catalyst surface, and more molecules tend to absorb the radicals as the concentration of MB increases. They eventually undergo photodegradation, which quickens the reaction's rate. The possible active sites on a given weight of the catalyst are restricted, even when the number of molecules grows with a further increase in the concentration of MB. Although the concentration of MB was raised, more molecules competed for the same number of active sites. Because MB is a large molecule, there are still unoccupied active sites even as the number of molecules grows in proportion to the concentration. The steric hindrance that prevents available MB molecules from reaching the catalyst's active sites reduces MB photodegradation.

4.10. The effect of co-pollutants

The effect of the co-pollutants on the photocatalytic activity was determined using Pb^{2+}, PO_4^{3-}, Cl^-, and Rhodamine B as the model pollutants representing heavy metals, fertilizers and pesticides, salts, and dyes, respectively (Fig. 13). The rate constant of photodegrading MB decreased to 2.01×10^{-3} min^{-1} from 3.8×10^{-3} min^{-1}. Pb^{2+} are positive ions but very small compared to the positive but bulky MB molecules. Hence, they easily reach the negatively charged catalyst sites and adsorb on the surface. MB molecules, which are bulky in nature, compete with Pb^{2+} ions and retard the migration to the catalyst surface; hence, with a smaller number of MB

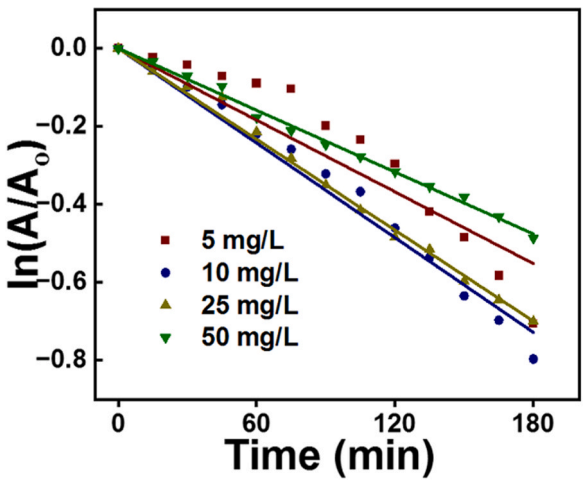

Fig. 12. The effect of the MB concentration on the photocatalysis.

molecules being adsorbed to the surface of the catalyst, the rate of the reaction of photodegrading MB decreases. There is no significant change in the reaction rate in the presence of PO_4^{3-} and Cl^-. Both are negatively charged ions without attraction to the negatively charged catalyst surface. Further, though they might have coupled with positively charged MB molecules due to their negative charge, such interaction does not affect the photodegradation of MB. The reaction rate has dropped to 2.85×10^{-3} min^{-1} in the presence of Rhodamine B (RhB), another textile dye, due to the competitive nature of both bulky dyes to the catalyst surface. Meanwhile, RhB has also been degraded with a rate constant of 1.25×10^{-3} min^{-1}. This supports our argument that the RhB molecules have also been adsorbed to the catalyst surface and degraded due to the radicals produced.

4.11. Mechanism

The band alignment of the heterostructure formed in the nanomaterials is essential to describe the photocatalysis mechanism. The band edge potentials of the conduction band (E_{CB}) and the valence band (E_{VB}) were calculated using the equations given below,

$$E_{CB} = X - E^C - 0.5\ E_g$$

$$E_{VB} = X - E^C + 0.5\ E_g$$

X is the electronegativity of the semiconductor, which is the geometric mean of the electronegativity of the constituent atoms, and E^C represents the energy of the free electrons on the hydrogen scale, approximately 4.5. The X values of CoO (Mei et al., 2021), Co_3O_4 (Huang et al., 2019), Mn3O4 (Rahimi et al., 2017) and Mn2O3 (Ghaffari et al., 2020) are 5.58, 5.42, 5.57 and 5.68, respectively. E_{CB} values of those oxides are 0.14, - 0.02, 0.14, and 0.24 eV/normal hydrogen electrode (NHE), respectively, and the E_{VB} values of those oxides are 2.02, 1.86, 2.02, and 2.12 eV/normal hydrogen electrode (NHE), respectively.The CoO_x sample contains the CoO and Co_3O_4 organized, forming a heterostructure of type II band alignment separating the CB and VB charges, as shown in Fig. 14 (a). Upon exposure to sunlight, an electron at the VB is excited to the CB of both the CoO and Co_3O_4, leaving a hole in the VB of the respective oxide semiconductors. The potential differences of the respective bands facilitate the movement of the charges between the semiconductors. The electron excited to the CB of Co_3O_4 moves to the CB of CoO, whereas a hole formed at the VB of CoO migrates to the VB of Co_3O_4, preventing the electron-hole pair recombination. Similarly, upon exposure to sunlight, an electron from each Mn_3O_4 and Mn_2O_3 gets excited to the CB, leaving a hole at the VB, and the electron excited to the CB of Mn_3O_4 moves to the CB of Mn_2O_3 while the hole created at the VB of Mn_2O_3 moves to the VB of Mn_3O_4 (Fig. 14 (b)). In the CM samples where the metal oxides are in a composite, but CoO is absent, as revealed by the XRD analysis, all three semiconductors, Co_3O_4, Mn_3O_4 and Mn_3O_4, are being excited when they are exposed to sunlight and electrons from their VB, are excited to the CB of the respective semiconductors. The potential of the VB of the semiconductors favours the migration of the holes from Mn_2O_3 to Mn_3O_4 and then to Co_3O_4, whereas the electrons at the CB of Co_3O_4 migrate to the CB of Mn_3O_4 and then to the CB of Mn_2O_3. This charge migration minimizes the electron-hole pair recombination, increasing the photocatalytic activity, as shown in Fig. 14 (c). When the metal oxide semiconductors are coupled with GO, the particular charges formed at the VB and the CB migrate on the conductive GO matrix, further separating the charges and facilitating the charge migration from one cluster of semiconductors to another (Fig. 14 (d)). Therefore, the incorporation of GO increases photocatalytic activity. The potential of the reduction of O_2 forming $O_2^{\bullet}$ is −0.33 eV, and the potential of the CB of all three metal oxide semiconductors Co_3O_4, Mn_3O_4 and Mn_2O_3 being greater than that facilitates the reduction of O_2 to $O_2^{\bullet}$. The potential of the reduction of OH^- to $OH^{\bullet}$ is 1.99 eV, and the potential of the VB of Mn_3O_4 and Mn_2O_3 being greater than that facilitates the reduction of OH^- to $OH^{\bullet}$ whereas the reaction is not favoured at the VB of Co_3O_4 due to its potential being lesser than the reduction potential of OH^- to $OH^{\bullet}$.

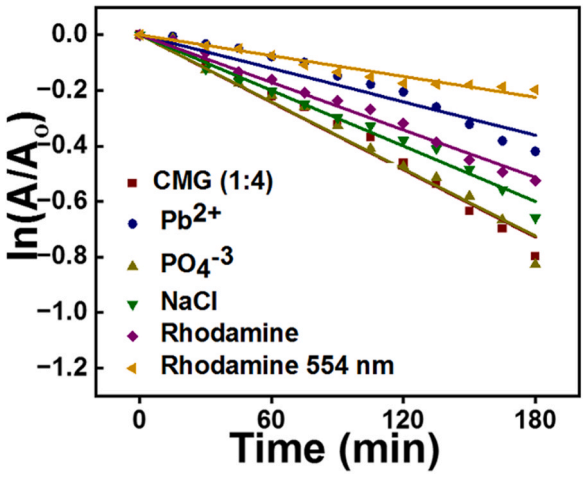

Fig. 13. The effect of co-pollutants on photocatalysis.

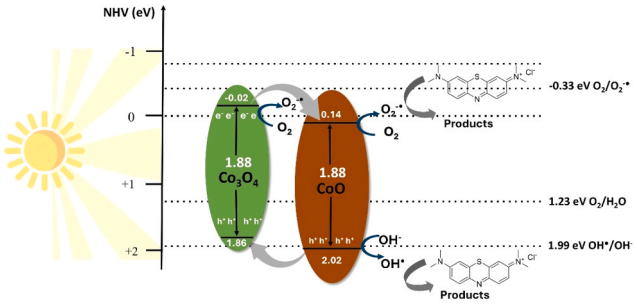

(a)

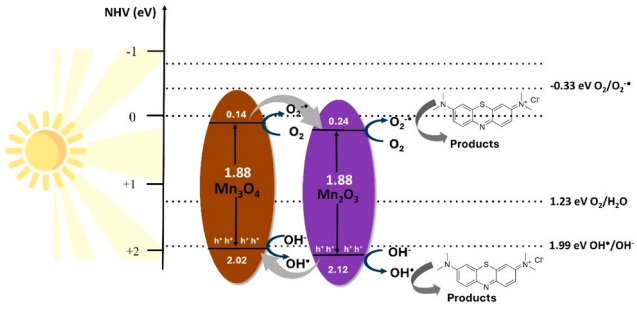

(b)

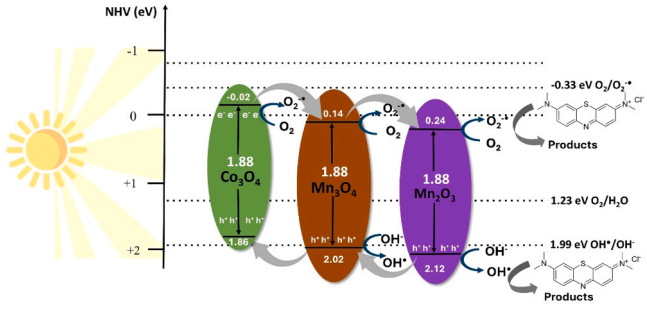

(c)

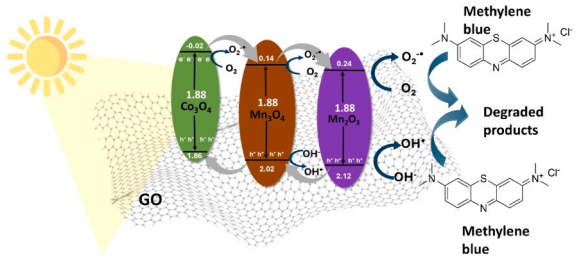

(d)

Fig. 14. Photocatalytic mechanism of degrading MB in the presence of (a) CoO_x (b) MnO_x (c) CoO_x-MnO_x and (d) CoO_x-MnO_x/GO.

4.12. Reusability

The reusability of the best-performing catalyst CMG (1:4) was investigated for five cycles, in which the catalyst was washed with ethanol and distilled water, followed by drying. The conversion of MB was observed to be reduced from 88 % to 72 %, as shown in Fig. 15. The activity is reduced at each cycle due to the unavailability of the active sites for the adsorption of MB on the catalyst and the graphene oxide, which is required for photocatalysis. This is due to the presence of chemisorbed MB molecules in the active sites as only loosely bound; more precisely, the physisorbed MB are removed upon washing with ethanol and distilled water. The porous structure is clogged with MB molecules, demarcating further adsorption and, hence, the photodegradation of MB molecules. The

catalyst, which is weighed to be 20 mg, could be lost at each cycle at washing, further contributing to the reduction of conversion. Moreover, the metal oxide nanocomposite catalyst could be leached from the GO matrix during the reaction and washing of the catalyst, which could eventually lead to a low conversion of MB moving from one cycle to another. Hence, the catalyst can be reused for several cycles but with some activity loss.

The photocatalytic activity of the best-performing catalyst (CMG (1:4)) was compared with similar catalysts reported in the literature (Table 4). It is worth noting that, supporting the novelty of this work, a similar catalyst was not found. However, the activity was compared to similar catalysts, where it was found that the photocatalytic activity was dependent on the dye concentration, the weight of the catalyst used, the light source and the catalyst itself. However, it was noted that there are catalysts whose performance is better than that of the best-performing catalyst, whereas the photocatalytic activity of some other catalysts is lesser than CMG (1:4). Hence, the fabricated catalyst possesses considerable photocatalytic activity compared to similar catalysts reported in the literature.

4.13. Antibacterial activity

Samples including GO, CoO_x, MnO_x, CoO_xG, MnO_xG, CM (1:1), CM (2:1), CM (4:1), CM (1:2), CM (1:4), CMG (1:1), CMG (2:1), CMG (4:1), CMG (1:2) and CMG (1:4) have shown substantial antibacterial activity against *Staphylococcus aureus*, *Escherichia coli*, *Klebsiella pneumoniae* and *Pseudomonas aeruginosa* at 20, 40 and 60 mg/ mL. The zone of inhibition of all four samples against the test organisms is shown in Fig. 16.

Across all samples, at the lowest concentration tested 20 mg/ mL, the highest zone of inhibitions was recorded for CoO_xG against *Staphylococcus aureus*, *Escherichia coli*, *Klebsiella pneumoniae* and *Pseudomonas aeruginosa* with 24.66 ± 0.33 mm, 21.00 ± 0.00 mm, 21.66 ± 0.67 mm and 20.0 ± 1.15 mm zones of inhibition respectively. At 60 mg/ mL, the highest antibacterial activity was recorded for CoO_xG against *Staphylococcus aureus*, *Escherichia coli*, *Klebsiella pneumoniae* and *Pseudomonas aeruginosa* with zone of inhibition values of 20.67 ± 0.33 mm, 19.00 ± 1.00 mm, 21.0 ± 0.58 mm and 22.67 ± 0.88 mm respectively. Similarly, at the highest concentration tested, CoO_xG provided the highest antibacterial activity for all samples except for *Staphylococcus aureus,* with a zone of inhibition of 20.67 ± 0.33 mm. Graphene oxide was incorporated into nanocomposites because it is widely used as an antibacterial agent for treating infections with multidrug resistance is increasing due to the distinctive physicochemical characteristics, such as large surface area, exceptional electrical and thermal conductivity, and compatibility with live biosystems. The two-dimensional (2D) layer of sp2-hybridized carbon atoms arranged in a honeycomb lattice, known as graphene, has shown significant use in the field of biotechnology. Graphene oxide-based nanocomposites have gained significant interest in many fields, including managing antimicrobial resistance in pathogens over recent years (Chen et al., 2013). Successful improvement of the antibacterial properties of graphene oxides (GOs) may be accomplished by integrating many functionalisation methods, as demonstrated in the present work. Numerous studies indicate that the antibacterial efficacy of graphene oxide is likely attributed to its large surface area, exceptional thermal stability, specific physiochemical characteristics, excellent electrical conductivity, and remarkable mechanical strength (Chen et al., 2013). Recent research indicates that the strong antibacterial effectiveness of graphene oxide is attributed to its ability to disrupt cell membranes by generating reactive oxygen species and its very sharp edges (Kang et al., 2007). The superiority of graphene oxide in terms of bactericidal or inhibitory effects compared to other antibacterial materials may be effectively outlined by three specific features: (i) The antibacterial mechanism of graphene oxide is influenced by both physical degradation and chemical oxidation, results in a reduction in bacterial resistance. (ii) Graphene oxide exhibits modest cytotoxicity against mammalian cells at low doses. (iii) Compared to other carbon nanomaterials, its ease of processing, large-scale manufacturing, and cheap production cost ensure its effectiveness as an antibacterial agent (Liu et al., 2008).

Interestingly, the zone of inhibition was highest at a value of 24.66 ± 0.33 mm against *Staphylococcus aureus* for CoO_xG out of all

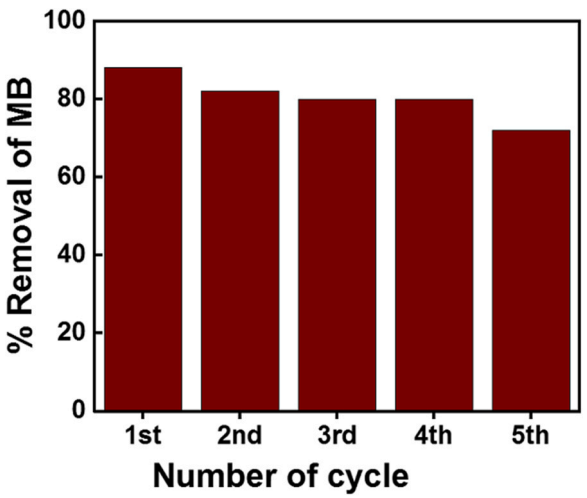

Fig. 15. The reusability study of the CMG (1:4) catalyst.

Table 4
Comparison of the catalytic performance of the best performing catalyst with similar catalysts in literature.

Photocatalyst	Dye	Concentration	Light source	Rate constant/Conversion	Reference
Co-Al LDH/GO	MB	10 mg/L	10 W LED light	8.905×10^{-1} min^{-1}	(Asif et al., 2022)
GCoO-NPs	Acid Blue−74	10 mg/L	450 W Xenon lamp	4.3 $x10^{-2}$ min^{-1}	(Samuel et al., 2020)
Co_3O_4–rGO	MB	5 mg/L	50 W LED solar light simulator	1.7 $x10^{-2}$ min^{-1}	(Bankole et al., 2020)
$MnFe_2O_4$/rGO	MB	10 mg/L	40 W UV lamp	5.8 $x10^{-2}$ min^{-1}	(Mandal et al., 2020)
Mn@Co_3O_4/rGO	MB	10 mg/L	Visible light	93.4 %	(Maqsood et al., 2023)
Mn_3O_4	Alizarin red	2.0 μM	Tungsten lamp	50 %	(Rahaman and Ghosh, 2016)
rGO/Mn_3O_4	MB	10 mg/L	Hg Lamp	21 %	(Mousa et al., 2020)
Mn_3O_4	MB	10 mg/L	UV lamp	38 %	(Rizal et al., 2021)
CMG (1:4)	MB	10 mg/L	Sunlight	3.5 $x10^{-3}$ min^{-1} (88 %)	This study

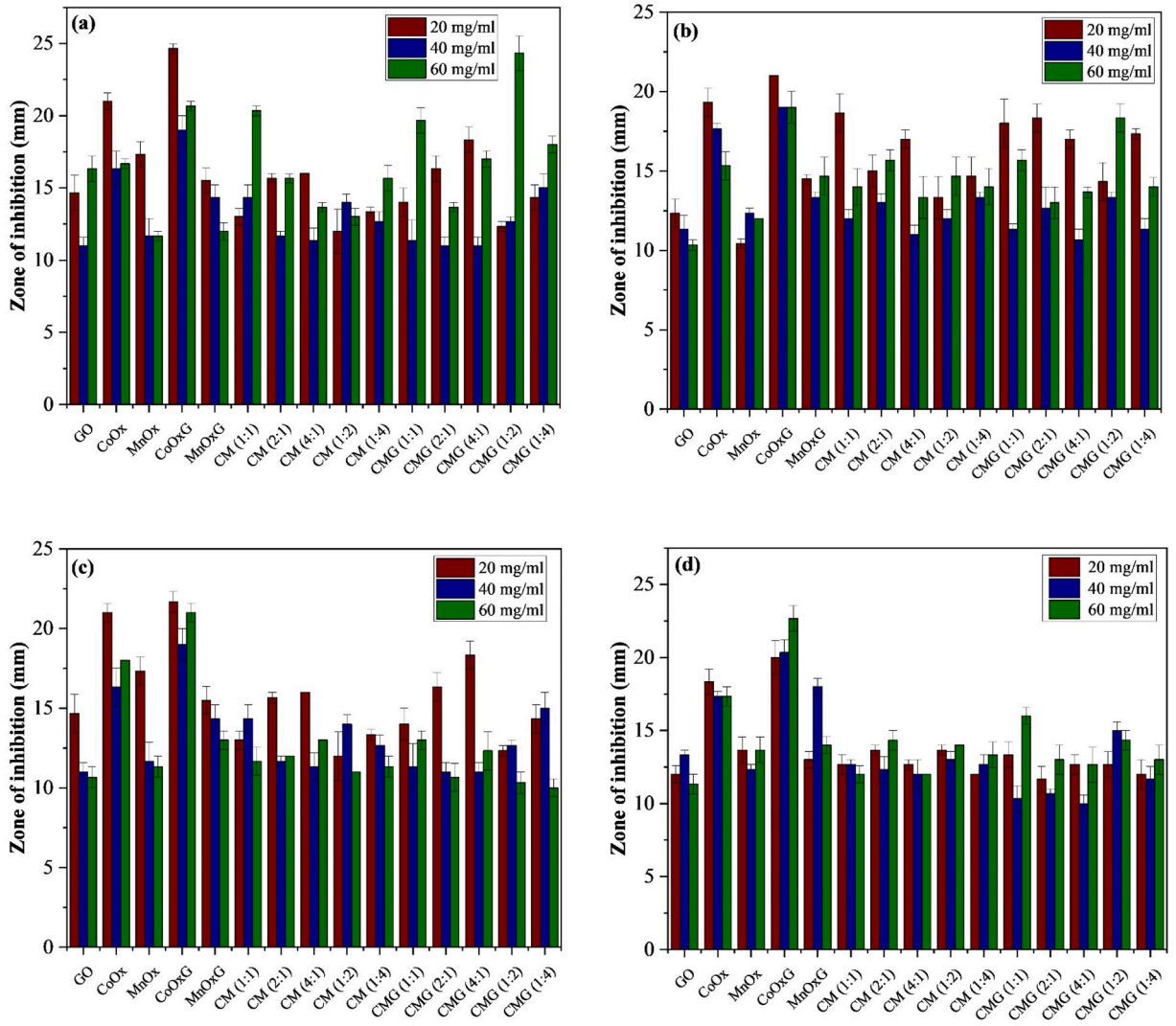

Fig. 16. The variation of the zone of inhibition with varying dosage of the catalysts on the inhibition of (a) *Staphylococcus aureus*, (b) *Escherichia coli*, (c) *Klebsiella pneumoniae* and (d) *Pseudomonas aeruginosa*.

newly synthesized nanocomposites at 20 mg/mL. As a transition metal oxide, cobalt oxide has distinctive features, including a large surface area resulting from its tiny size, strong magnetic behaviour, and exceptional catalytic activities (Dey and Dhal, 2019). Cobalt nanoparticles are well-recognised for their elevated melting point, resistance to oxidation, and unique magnetic characteristics (Barakat et al., 2009). It is found to be extensively used in industrial technologies like magnetic tape, chemical catalysis, gas sensing

equipment, coating, and light absorption, as well as in medical biotechnology for magnetic resonance imaging. A wide variety of applications, including energy, water treatment, medicinal, and antibacterial, have used Cobalt Oxide nanoparticles (Adino et al., 2021). The antimicrobial characteristics of these nanoparticles are thought to stem from their capacity to produce reactive oxygen species (ROS) that may harm bacterial cell membranes and impede bacterial proliferation (Saravanan et al., 2021b). Reactive oxygen species (ROS) are oxygen-containing chemically reactive particles, such as hydrogen peroxide (H2O2), reactive superoxide anion radicals (O2-), and hydroxyl radicals ($OH^{\bullet}$). The generation of reactive oxygen species (ROS) is mostly seen in organelles, including the endoplasmic reticulum (ER), peroxisomes, and particularly in the mitochondria. In oxidative phosphorylation, oxygen is used to produce water by donating electrons via the mitochondrial electron transport chain (ETC). A portion of these electrons are absorbed by molecular oxygen to generate O2-, which may subsequently convert H_2O_2 and $OH^{\bullet}$ groups (Boonstra and Post, 2004; Murphy, 2009).

The surplus production of reactive oxygen species (ROS) may lead to many physiological and pathological consequences, including genotoxicity, apoptosis, necrosis, inflammation, fibrosis, metaplasia, hypertrophy, and carcinogenesis (AshaRani et al., 2012). Further studies have shown that the toxicity of nanoparticles may augment the production of pro-inflammatory cytokines and stimulate inflammatory cells, including macrophages, thereby promoting the creation of reactive oxygen species (ROS). The elevated production of reactive oxygen species (ROS) after exposure to nanoparticles (NPs) has also been shown to cause the alteration of cellular processes, leading to lethal outcomes in some instances (Patlolla et al., 2015).

The highest zone of inhibition recorded for MnO_xG was 18.0 ± 0.58 mm against *Staphylococcus aureus*. All the Mn-incorporated samples have demonstrated substantial antibacterial activity against all four pathogens tested. Manganese is known to contain high levels of antimicrobial attributes. Manganese oxide nanoparticles have effective properties that combat antibacterial resistance through several mechanisms. Through their interaction with thiol groups of proteins, disruption of bacterial membranes, and disruption of DNA replication, nanoparticles are able to penetrate bacterial cells and function as a catalyst to deactivate enzymes necessary for microbial metabolism. Nanoparticles having a higher surface-to-volume ratio may demonstrate enhanced antibacterial efficacy by penetrating biofilms and bacterial cell walls, therefore inducing cytotoxicity due to their nanoscale dimensions (Jayanetti et al., 2024; Alavi and Rai, 2019). The synergistic effect of the combination of Copper and Manganese oxide nanomaterials has led to this increased antibacterial activity. The synergistic effect has enhanced the overall inhibition to optimize the molecular interactions between bacterial cells and nanocomposites and the bactericidal effects of the nanocomposite on the application site.

Furthermore, at all tested concentrations, namely 20, 40 and 60 mg/ mL, the lowest zone of inhibition recorded was below 11.00 ± 0.00 mm across all samples against *Escherichia coli*, *Klebsiella pneumoniae* and *Pseudomonas aeruginosa. Staphylococcus aureus* showed the least resistance towards samples tested, 11.00 ± 0.58 mm being the lowest zone of inhibition recorded for any sample. Therefore, it can be considered as the most sensitive pathogen out of the tested strains.

Overall, the metal oxide nanocomposites showed more sensitivity towards the Gram-positive strain *Staphylococcus aureus* compared

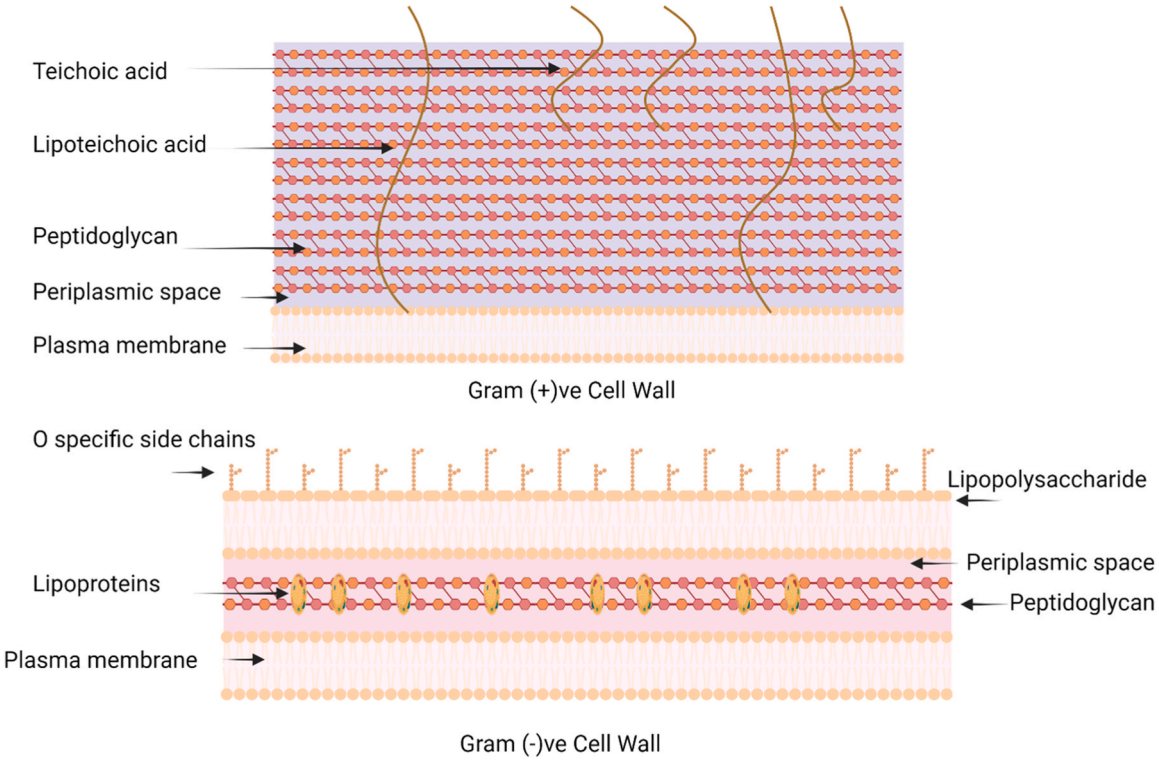

Fig. 17. Illustration of the cell walls of Gram-positive and Gram-negative bacteria.

to the Gram-negative bacteria *Escherichia coli, Pseudomonas aeruginosa,* and *Klebsiella pneumoniae* across all samples tested. Outlining the differences in the cell walls of Gram-positive and Gram-negative bacteria is essential since the main toxicological impact of antimicrobial drugs on bacteria occurs when they directly interact with the cell surface. Fig. 17 illustrates the structure of the cell walls of Gram-positive and Gram-negative bacteria. The bacterial surface, whether Gram-positive or Gram-negative, carries a negative charge. The peptidoglycan layer of gram-positive bacteria consists of alternating N-acetylglucosamine (NAG) and N-acetylmuramic acid (NAM) residues arranged in linear chains. The chains are interconnected by a configuration of 3–5 amino acids that covalently bind to create a seamless network. Gram-positive bacteria often possess negatively charged teichoic acids, which are characterized by significant phosphate groups extending from the cell wall to the surface. Gram-negative bacteria, in contrast, possess a far more intricate structure. Gram-negative bacteria possess an external membrane composed of phospholipids and partially phosphorylated lipopolysaccharides (LPS), along with a sparse peptidoglycan coating, which augment the negative surface charge of their cell envelope (Bruslind, 2017). Moreover, metal ions have been reported to disrupt the integrity of the cell wall and cytoplasmic membrane in Gram-negative and positive bacteria (Jayanetti et al., 2024). Upon entering the bacterial cell, they induce denaturation of the ribosomes, disrupting protein synthesis. Moreover, the presence of metal ions would disrupt the process of ATP synthesis since they deactivate respiratory enzymes located on the cytoplasmic membrane. The above-mentioned mechanisms are illustrated in Fig. 18.

5. Conclusions

CoO_x and MnO_x nanoparticles, composites of varying weight ratios as 4:1, 2:1, 1:1, 1:2 and 1:4, and composites coupled with 30 % (weight) GO were successfully fabricated. The composites were visible light sensitive, irregularly shaped nanoparticles of a combination of Co_3O_4, Mn_2O_3 and Mn_3O_4, which are heterogeneously distributed on the GO matrix. Adsorption of MB to the synthesized nanomaterials followed pseudo second-order kinetics, suggesting the chemisorption of Mb to the adsorbents. The total removal of MB significantly increased with the incorporation of GO. The synthesized nanomaterials were photocatalytically active in degrading MB under sunlight. The presence of $S_2O_8^{2-}$ increased the reaction rate, while the presence of scavengers like EDTA and IPA decreased the reaction rate. The reaction rate generally increased with the increasing weight of the catalyst and decreased with the increase in MB concentration. The best-performing catalyst successfully degraded MB for five consecutive cycles with some activity loss. The nanomaterials were effective in creating an inhibitory effect on *Escherichia coli*, *Klebsiella pneumoniae*, *Pseudomonas aeruginosa* and *Staphylococcus aureus* being more sensitive to the Gram-positive strain than the Gram-negative strains in all tested samples.

Funding statement

This research was supported by the Accelerating Higher Education Expansion and Development (AHEAD) Operation of the Ministry

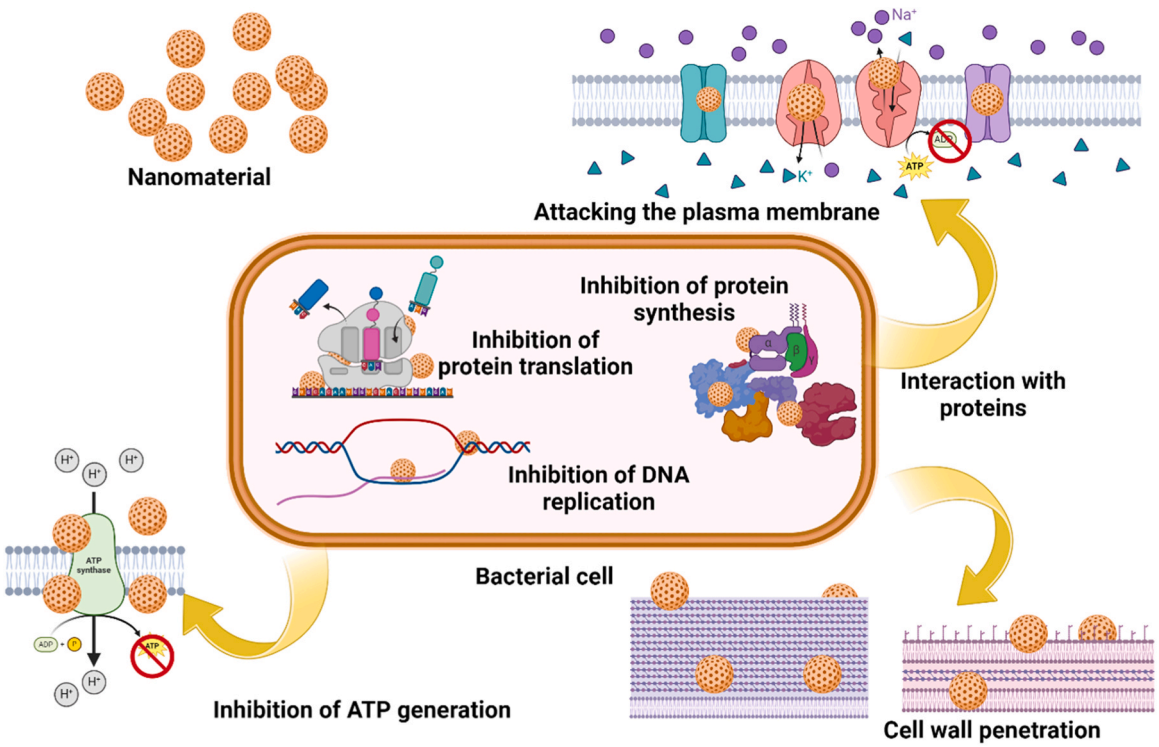

Fig. 18. A schematic representation depicting the interactions between nanoparticles and bacterial cells.

of Higher Education, funded by the World Bank.

CRediT authorship contribution statement

Charitha Thambiliyagodage: Writing – review & editing, Writing – original draft, Validation, Supervision, Resources, Project administration, Funding acquisition, Conceptualization. **Heshan Liyanaarachchi:** Methodology, Investigation, Formal analysis, Data curation, Conceptualization. **Madara Jayanetti:** Writing – original draft, Methodology, Investigation. **Geethma Ekanayake:** Writing – original draft, Methodology, Investigation. **Supuni Wijayawardana:** Writing – original draft, Software, Formal analysis. **Upeka Samarakoon:** Resources.

Declaration of Competing Interest

The authors declare that they have no known competing financial interests or personal relationships that could have appeared to influence the work reported in this paper.

Acknowledgement

The authors acknowledge the Sri Lanka Institute of Nanotechnology and the University of Moratuwa for providing instrument facilities

Appendix A. Supporting information

Supplementary data associated with this article can be found in the online version at doi:10.1016/j.eti.2024.103984.

Data Availability

Data will be made available on request.

References

Abdel-Fatah, M.A., 2018. Nanofiltration systems and applications in wastewater treatment: review article. Ain Shams Eng. J. 9 (4), 3077–3092.
Adino, A.T., Edosa, G.D., Gonfa, B.A., Bekele, E.T., Sabir, F.K., 2021. Synthesis of cobalt oxide nanoparticles through chemical and biological pathways for antibacterial activity. J. Nanostruct. 11 (3), 577–587.
Alavi, M., Rai, M., 2019. Recent advances in antibacterial applications of metal nanoparticles (MNPs) and metal nanocomposites (MNCs) against multidrug-resistant (MDR) bacteria. Expert Rev. Anti Infect. Ther. 17 (6), 419–428.
Al-Gheethi, A.A., Efaq, A.N., Bala, J.D., Norli, I., Abdel-Monem, M.O., Ab. Kadir, M.O., 2018. Removal of pathogenic bacteria from sewage-treated effluent and biosolids for agricultural purposes. Appl. Water Sci. 8 (2), 1–25.
Al-Tohamy, R., Ali, S.S., Li, F., Okasha, K.M., Mahmoud, Y.A.G., Elsamahy, T., et al., 2022. A critical review on the treatment of dye-containing wastewater: ecotoxicological and health concerns of textile dyes and possible remediation approaches for environmental safety. Ecotoxicol. Environ. Saf. 231, 113160.
Amin, M.T., Alazba, A.A., Manzoor, U., 2014. A review of removal of pollutants from water/wastewater using different types of nanomaterials. Adv. Mater. Sci. Eng. 2014, 1–24. Available from: ⟨http://www.hindawi.com/journals/amse/2014/825910/⟩.
Anis, S.F., Hashaikeh, R., Hilal, N., 2019. Microfiltration membrane processes: a review of research trends over the past decade. J. Water Process Eng. 32, 100941.
AshaRani, P.V., Sethu, S., Lim, H.K., Balaji, G., Valiyaveettil, S., Hande, M.P., 2012. Differential regulation of intracellular factors mediating cell cycle, DNA repair and inflammation following exposure to silver nanoparticles in human cells. Genome Integr. 3 (1), 1–14.
Asif, M., Saeed, M., Zafar, M., Amjad, U., e, Razzaq, S., Kim, A., 2022. WY. Development of Co-Al LDH/GO composite photocatalyst for enhanced degradation of textile pollutant under visible light irradiation. Results Phys. 42, 105997. Available from: ⟨https://www.sciencedirect.com/science/article/pii/S2211379722006118⟩.
Aslam, M., Qamar, M.T., Rehman, A.U., Soomro, M.T., Ali, S., Ismail, I.M.I., et al., 2018. The evaluation of the photocatalytic activity of magnetic and non-magnetic polymorphs of Fe 2 O 3 in natural sunlight exposure: a comparison of photocatalytic activity. Appl. Surf. Sci. 451, 128–140.
Bankole, O.M., Olaseni, S.E., Adeyemo, M.A., Ogunlaja, A.S., 2020. Microwave-assisted synthesis of cobalt oxide/reduced graphene oxide (Co3O4–rGo) composite and its sulfite enhanced photocatalytic degradation of organic dyes, 234 (10), 1681–1708. https://doi.org/10.1515/zpch-2019-1524.
Barakat, N.A.M., Kim, B., Yi, C., Jo, Y., Jung, M.H., Chu, K.H., et al., 2009. Influence of cobalt nanoparticles' incorporation on the magnetic properties of the nickel nanofibers: cobalt-doped nickel nanofibers prepared by electrospinning. J. Phys. Chem. C. 113 (45), 19452–19457.
Bello, M.M., Abdul Raman, A.A., Asghar, A., 2019. A review on approaches for addressing the limitations of Fenton oxidation for recalcitrant wastewater treatment. Process Saf. Environ. Prot. 126, 119–140.
Bhuiyan, M.S.H., Miah, M.Y., Paul, S.C., Aka, T.Das, Saha, O., Rahaman, M.M., et al., 2020. Green synthesis of iron oxide nanoparticle using Carica papaya leaf extract: application for photocatalytic degradation of remazol yellow RR dye and antibacterial activity. Heliyon 6 (8), e04603. Available from: ⟨https://www.sciencedirect.com/science/article/pii/S240584402031447X⟩.
Boonstra, J., Post, J.A., 2004. Molecular events associated with reactive oxygen species and cell cycle progression in mammalian cells. Gene 337, 1–13.
Bruslind, L., 2017. Microbiology. Open Oregon State.
Cabral, J.P.S., 2010. Water microbiology. Bacterial pathogens and water, 2010, Vol 7, Pages 3657-3703 Int J. Environ. Res Public Heal 7 (10), 3657–3703.
Camcioglu, S., Pekel, L.C., Polat, K., Hapoglu, H., 2014. Experimental design of wastewater treatment with electro-coagulation. Manag Environ. Qual. Int J. 25 (1), 86–95.
Che, M., Bennett, C.O., 1989. In: Eley, D.D., Pines, H., Weisz, P.B.B.T.A. in C. (Eds.), The Influence of Particle Size on the Catalytic Properties of Supported Metals. Academic Press, pp. 55–172. Available from: ⟨https://www.sciencedirect.com/science/article/pii/S0360056408600176⟩.
Chen, J., Wang, X., Han, H., 2013. A new function of graphene oxide emerges: Inactivating phytopathogenic bacterium Xanthomonas oryzae pv. Oryzae. J. Nanopart. Res 15 (5), 1–14.

D. Stickland, A.D., Burgess, C., Dixon, D.R., Harbour, P.J., Scales, P.J., Studer, L.J., et al., 2008. Fundamental dewatering properties of wastewater treatment sludges from filtration and sedimentation testing. Chem. Eng. Sci. 63 (21), 5283–5290.
Dai, G., Liu, S., Liang, Y., 2014. A simple preparation of carbon doped porous Bi2O3 with enhanced visible-light photocatalytic activity. J. Alloy. Compd. 608, 44–48.
Dai, Y., Men, Y., Wang, J., Liu, S., Li, S., Li, Y., et al., 2021. Tailoring the morphology and crystal facet of Mn3O4 for highly efficient catalytic combustion of ethanol. Colloids Surf. A Physicochem Eng. Asp. 627, 127216.
Dey, S., Dhal, G.C., 2019. The catalytic activity of cobalt nanoparticles for low-temperature oxidation of carbon monoxide. Mater. Today Chem. 14.
Faheem, M., Iqbal, T., Afsheen, S., Basit, A., Munir, R.M., Khan, M.I., et al., 2024. A maghemite (γ-Fe2O3) incorporated activated carbon photocatalytic nanocomposite fabricated via Co-precipitation utilized against degradation of methyl orange. Opt. Mater. (Amst.) 157, 116131. Available from: ⟨https://www.sciencedirect.com/science/article/pii/S0925346724013144⟩.
Garrido-Cardenas, J.A., Esteban-García, B., Agüera, A., Sánchez-Pérez, J.A., Manzano-Agugliaro, F., 2019. Wastewater treatment by advanced oxidation process and their worldwide research trends. Int. J. Environ. Res. Public Heal 17 (1), 170.
Ghaffari, Y., Gupta, N.K., Bae, J., Kim, K.S., 2020. One-step fabrication of Fe2O3/Mn2O3 nanocomposite for rapid photodegradation of organic dyes at neutral pH. J. Mol. Liq. 315, 113691.
Ghorai, T.K., Dhak, D., Dalai, S., Pramanik, P., 2008. Preparation and photocatalytic activity of nano-sized nickel molybdate (NiMoO4) doped bismuth titanate (Bi2Ti4O11) (NMBT) composite. J. Alloy. Compd. 463 (1–2), 390–397.
Ghosh, M., Liu, J., Chuang, S.S.C., Jana, S.C., 2018. Fabrication of hierarchical V2O5 nanorods on TiO2 nanofibers and their enhanced photocatalytic activity under visible light. ChemCatChem 10 (15), 3305–3318. Available from: ⟨https://onlinelibrary.wiley.com/doi/full/10.1002/cctc.201800172⟩.
Gouvêa, C.A.K., Wypych, F., Moraes, S.G., Durán, N., Nagata, N., Peralta-Zamora, P., 2000. Semiconductor-assisted photocatalytic degradation of reactive dyes in aqueous solution. Chemosphere 40 (4), 433–440.
Greczynski, G., Hultman, L., 2020. X-ray photoelectron spectroscopy: towards reliable binding energy referencing. Prog. Mater. Sci. 107, 100591.
Guo, Y., Yang, X., Ma, F., Li, K., Xu, L., Yuan, X., et al., 2010. Additive-free controllable fabrication of bismuth vanadates and their photocatalytic activity toward dye degradation. Appl. Surf. Sci. 256 (7), 2215–2222.
Haunold, T., Rupprechter, G., 2021. LiOx-modification of Ni and Co3O4 surfaces: an XPS, LEIS and LEED study. Surf. Sci. 713, 121915.
Huang, R., Huang, S., Chen, D., Zhang, Q., Le, T.T., Wang, Q., et al., 2019. Environmentally benign synthesis of Co3O4-SnO2 heteronanorods with efficient photocatalytic performance activated by visible light. J. Colloid Interface Sci. 542, 460–468.
Hübner, U., Spahr, S., Lutze, H., Wieland, A., Rüting, S., Gernjak, W., et al., 2024. Advanced oxidation processes for water and wastewater treatment – guidance for systematic future research. Heliyon 10 (9), e30402.
Iqbal, T., Afzal, M., Al- Asbahi, B.A., Afsheen, S., Maryam, I., Mssssushtaq, A., et al., 2024. Enhancing apple shelf life: A comparative analysis of photocatalytic activity in pure and manganese-doped ZnO nanoparticles. Mater. Sci. Semicond. Process 173, 108152. Available from: ⟨https://www.sciencedirect.com/science/article/pii/S1369800124000477⟩.
Jamjoum, H.A.A., Umar, K., Adnan, R., Razali, M.R., Mohamad Ibrahim, M.N., 2021. Synthesis, characterization, and photocatalytic activities of graphene oxide/metal oxides nanocomposites: a review. Front. Chem. 9, 752276.
Jayanetti, M., Thambiliyagodage, C., Liyanaarachchi, H., Ekanayake, G., Mendis, A., Usgodaarachchi, L., 2024. In vitro influence of PEG functionalized ZnO–CuO nanocomposites on bacterial growth. Sci. Rep. 14 (1), 1–21. Available from: ⟨https://www.nature.com/articles/s41598-024-52014-6⟩.
Kang, Y., João, S.M., Lin, R., Liu, K., Zhu, L., Fu, J., et al., 2024. Effect of crystal facets in plasmonic catalysis. Nat. Commun. 15 (1), 3923. https://doi.org/10.1038/s41467-024-47994-y.
Kang, S., Pinault, M., Pfefferle, L.D., Elimelech, M., 2007. Single-walled carbon nanotubes exhibit strong antimicrobial activity. Langmuir 23 (17), 8670–8673.
Khajouei, G., Finklea, H.O., Lin, L.S., 2022. UV/chlorine advanced oxidation processes for degradation of contaminants in water and wastewater: a comprehensive review. J. Environ. Chem. Eng. 10 (3), 107508.
Konsolakis, M., 2016. Surface chemistry and catalysis. Catalysts 6.
Kumari, P., Kumar, A., 2023 May. Advanced oxidation process: a remediation technique for organic and non-biodegradable pollutant. Results Surf. Interfaces 11, 100122.
La Cruz, A.M.De, Lozano, L.G.G., 2010. Photoassisted degradation of organic dyes by β-Bi2Mo 2O9. React. Kinet. Mech. Catal. 99 (1), 209–215.
Liu, H., Peng, T., Ke, D., Peng, Z., Yan, C., 2007. Preparation and photocatalytic activity of dysprosium doped tungsten trioxide nanoparticles. Mater. Chem. Phys. 104 (2–3), 377–383.
Liu, Z., Robinson, J.T., Sun, X., Dai, H., 2008. PEGylated nanographene oxide for delivery of water-insoluble cancer drugs. J. Am. Chem. Soc. 130 (33), 10876–10877.
Ma, D., Yi, H., Lai, C., Liu, X., Huo, X., An, Z., et al., 2021. Critical review of advanced oxidation processes in organic wastewater treatment. Chemosphere 275, 130104.
Mandal, B., Panda, J., Paul, P.K., Sarkar, R., Tudu, B., 2020. MnFe2O4 decorated reduced graphene oxide heterostructures: Nanophotocatalyst for methylene blue dye degradation. Vacuum 173, 109150. Available from: ⟨https://www.sciencedirect.com/science/article/pii/S0042207X19324042⟩.
Maqsood, J., Fallatah, A.M., Zaki, Z.I., Akhtar, M., Irshad, A., 2023. Manganese doped Co3O4/rGO nanocomposite: synthesis, characterisation and visible light irradiated photocatalytic degradation of methylene blue studies. Z. Phys. Chem. 237 (10), 1505–1523.
Martínez-de la Cruz, A., Obregón Alfaro, S., 2010. Synthesis and characterization of γ-Bi2MoO6 prepared by co-precipitation: photoassisted degradation of organic dyes under vis-irradiation. J. Mol. Catal. A Chem. 320 (1–2), 85–91.
Mei, F., Zhang, J., Liang, C., Dai, K., 2021. Fabrication of novel CoO/porous graphitic carbon nitride S-scheme heterojunction for efficient CO2 photoreduction. Mater. Lett. 282, 128722.
Mendis, A., Thambiliyagodage, C., Ekanayake, G., Liyanaarachchi, H., Jayanetti, M., Vigneswaran, S., 2023. Fabrication of naturally derived chitosan and ilmenite sand-based TiO2/Fe2O3/Fe-N-doped graphitic carbon composite for photocatalytic degradation of methylene blue under sunlight. Molecules 28 (7), 3154.
Mousa, M.A., Rashad, M.M., Mokhtar, M.M., El Shazli, M.E., 2020. Synthesis, characterization and photocatalytic activity of visible-light-driven Mn3O4 and reduced graphene oxide-Mn3O4 nanocomposite. J. Basic Environ. Sci. 7 (3), 171–184.
Mulyanti, R., Susanto, H., 2018. Wastewater treatment by nanofiltration membranes. IOP Conf. Ser. Earth Environ. Sci. 142 (1), 012017.
Murphy, M.P., 2009. How mitochondria produce reactive oxygen species. Biochem J. 417 (1), 1–13.
Nair, G., Soni, B., Shah, M., 2023. A comprehensive review on electro-oxidation and its types for wastewater treatment. Ground Sustain Dev. 23, 100980.
Natarajan, S., Bajaj, H.C., Tayade, R.J., 2018. Recent advances based on the synergetic effect of adsorption for removal of dyes from waste water using photocatalytic process. J. Environ. Sci. 65, 201–222.
Pandey, P.K., Kass, P.H., Soupir, M.L., Biswas, S., Singh, V.P., 2014. Contamination of water resources by pathogenic bacteria. AMB Express 4 (1), 1–16.
Patidar, R., Srivastava, V.C., 2021. Evaluation of the sono-assisted photolysis method for the mineralization of toxic pollutants. Sep Purif. Technol. 258, 117903.
Patlolla, A.K., Hackett, D., Tchounwou, P.B., 2015. Silver nanoparticle-induced oxidative stress-dependent toxicity in Sprague-Dawley rats. Mol. Cell Biochem. 399 (1–2), 257–268.
Qin, J., Zhang, X., Yang, C., Cao, M., Ma, M., Liu, R., 2017. ZnO microspheres-reduced graphene oxide nanocomposite for photocatalytic degradation of methylene blue dye. Appl. Surf. Sci. 392, 196–203.
Rahaman, H., Ghosh, S.K., 2016. Soft-templated synthesis of Mn3O4 microdandelions for the degradation of alizarin red under visible light irradiation. RSC Adv. 6 (6), 4531–4539. https://doi.org/10.1039/C5RA25935E.
Rahimi, R., Mehrehjedy, A., Zargari, S., 2017. BiVO4/Mn3O4 a novel p–n heterojunction photocatalyst functionalized with metalloporphyrins: synthesis, charge transfer mechanism, and enhanced visible-light photocatalysis for degradation of dye pollutant. Environ. Prog. Sustain Energy 36 (5), 1439–1448.
Rashid, R., Shafiq, I., Akhter, P., Iqbal, M.J., Hussain, M., 2021. A state-of-the-art review on wastewater treatment techniques: the effectiveness of adsorption method. Environ. Sci. Pollut. Res 28 (8), 9050–9066. Available from: ⟨https://link.springer.com/article/10.1007/s11356-021-12395-x⟩.

Rizal, M.Y., Saleh, R., Prakoso, S.P., Taufik, A., Yin, S., 2021. Ultraviolet- and visible-light photocatalytic and sonophotocatalytic activities toward Congo red degradation using Ag/Mn3O4 nanocomposites. Mater. Sci. Semicond. Process 121, 105371. Available from: ⟨https://www.sciencedirect.com/science/article/pii/S136980012031307X⟩.

Rizvi, H.I., Munir, R.M., Iqbal, T., Younas, A., Afsheen, S., Qureshi, M.T., et al., 2024. Novel existence of Mn and Cu in WO3 nanostructures for promising photocatalytic activity against MB dye and Levofloxacin antibiotic. J. Alloy. Compd. 993, 174549. Available from: ⟨https://www.sciencedirect.com/science/article/pii/S0925838824011368⟩.

Roy, N., Chakraborty, S., 2021. ZnO as photocatalyst: an approach to waste water treatment. Mater. Today Proc. 46, 6399–6403.

Saba, B., Kjellerup, B.V., Christy, A.D., 2021. Eco-friendly bio-electro-degradation of textile dyes wastewater. Bioresour. Technol. Rep. 15, 100734.

Samuel, M.S., Selvarajan, E., Mathimani, T., Santhanam, N., Phuong, T.N., Brindhadevi, K., et al., 2020. Green synthesis of cobalt-oxide nanoparticle using jumbo Muscadine (Vitis rotundifolia): Characterization and photo-catalytic activity of acid Blue-74. J. Photochem. Photobio. B Biol. 211, 112011. Available from: ⟨https://www.sciencedirect.com/science/article/pii/S1011134420304619⟩.

Saravanan, A., Maruthapandi, M., Das, P., Luong, J.H.T., Gedanken, A., 2021b. Green synthesis of multifunctional carbon dots with antibacterial activities. Nanomater 11 (2), 369.

Saravanan, A., Senthil Kumar, P., Jeevanantham, S., Karishma, S., Tajsabreen, B., Yaashikaa, P.R., et al., 2021a. Effective water/wastewater treatment methodologies for toxic pollutants removal: processes and applications towards sustainable development. Chemosphere 280, 130595.

Shi, M., Li, W., Wang, Q., Xu, H., Zhao, Y., He, G., et al., 2021. One-step hydrothermal synthesis of BiVO4/TiO2/RGO composite with effective photocatalytic performance for the degradation of ciprofloxacin. Opt. Mater. (Amst.) 122, 111726.

Siagian, U.W.R., Khoiruddin, K., Wardani, A.K., Aryanti, P.T.P., Widiasa, I.N., Qiu, G., et al., 2021. High-performance ultrafiltration membrane: recent progress and its application for wastewater treatment. Curr. Pollut. Rep. 7 (4), 448–462.

Singh, P., Shandilya, P., Raizada, P., Sudhaik, A., Rahmani-Sani, A., Hosseini-Bandegharaei, A., 2020. Review on various strategies for enhancing photocatalytic activity of graphene based nanocomposites for water purification. Arab J. Chem. 13 (1), 3498–3520.

Subha, N., Mahalakshmi, M., Monika, S., Senthil kumar, P., Preethi, V., Vaishnavi, G., et al., 2022. Heterostructured γ-Fe2O3/FeTiO3 magnetic nanocomposite: an efficient visible-light-driven photocatalyst for the degradation of organic dye. Chemosphere 306, 135631.

Teh, C.Y., Budiman, P.M., Shak, K.P.Y., Wu, T.Y., 2016. Recent advancement of coagulation-flocculation and its application in wastewater treatment. Ind. Eng. Chem. Res. 55 (16), 4363–4389.

Thambiliyagodage, C.J., Cooray, V.Y., Perera, I.N., Wijesekera, R.D., 2020. Eco-Friendly Porous Carbon Materials for Wastewater Treatment. Springer, Singapore, pp. 252–260. Available from: ⟨http://link.springer.com/10.1007/978-981-13-9749-3_23⟩.

Thambiliyagodage, C., Liyanaarachchi, H., Jayanetti, M., Ekanayake, G., Mendis, A., Samarakoon, U., et al., 2024. Persulfate assisted photocatalytic and antibacterial activity of TiO2–CuO coupled with graphene oxide and reduced graphene oxide. Sci. Rep. 14 (1), 1–23.

Thambiliyagodage, C., Usgodaarachchi, L., Jayanetti, M., Liyanaarachchi, C., Kandanapitiye, M., Vigneswaran, S., 2022. Efficient visible-light photocatalysis and antibacterial activity of TiO2-Fe3C-Fe-Fe3O4/graphitic carbon composites fabricated by catalytic graphitization of sucrose using natural ilmenite. ACS Omega 7 (29), 25403–25421. Available from: ⟨https://pubs.acs.org/doi/full/10.1021/acsomega.2c02336⟩.

Tian, H., Zeng, L., Huang, Y., Ma, Z., Meng, G., Peng, L., et al., 2020. In situ electrochemical Mn(III)/Mn(IV) generation of Mn(II)O electrocatalysts for high-performance oxygen reduction. Nano-Micro Lett. 12 (1), 161.

Trishitman, D., Cassano, A., Basile, A., Rastogi, N.K., 2020. Reverse osmosis for industrial wastewater treatment. Curr Trends Futur Dev Membr Reverse Forw Osmosis Princ Appl Adv. 207–228.

Usgodaarachchi, L., Jayanetti, M., Thambiliyagodage, C., Liyanaarachchi, H., Vigneswaran, S., 2022. Fabrication of r-GO/GO/α-Fe2O3/Fe2TiO5 nanocomposite using natural ilmenite and graphite for efficient photocatalysis in visible light. Mater 16 (1), 139. Available from: ⟨https://www.mdpi.com/1996-1944/16/1/139/htm⟩.

Wang, J., Chen, H., 2020. Catalytic ozonation for water and wastewater treatment: recent advances and perspective. Sci. Total Environ. 704, 135249.

Younas, A., Munir, R.M., Rizvi, H.I., Iqbal, T., Afsheen, S., Riaz, K.N., et al., 2024. Novel S–N/WO3: Optimization of photocatalytic performance of WO3 by simultaneous existence of S and N in WO3 against MB dye. J. Chem. Phys. 160 (24), 244201. https://doi.org/10.1063/5.0213551.

Zawadzki, P., 2022. Visible light–driven advanced oxidation processes to remove emerging contaminants from water and wastewater: a review. Water Air Soil Pollut. 233 (9), 1–38, 2339. 2022 Sep.

Zhang, Y., Hou, X., Sun, T., Zhao, X., 2017. Calcination of reduced graphene oxide decorated TiO2 composites for recovery and reuse in photocatalytic applications. Ceram. Int. 43 (1), 1150–1159.

Zhang, X., Lv, X., Bi, F., Lu, G., Wang, Y., 2020. Highly efficient Mn2O3 catalysts derived from Mn-MOFs for toluene oxidation: the influence of MOFs precursors. Mol. Catal. 482, 110701.

Zhao, C., Zhou, J., Yan, Y., Yang, L., Xing, G., Li, H., et al., 2021. Application of coagulation/flocculation in oily wastewater treatment: a review. Sci. Total Environ. 765, 142795.